

# Geochemistry, Geophysics, Geosystems®



## RESEARCH ARTICLE

10.1029/2024GC011646

### Key Points:

- Paleomicrobial activity attested in the deep subsurface of Western Greenland
- Microbial sulfate reduction suggested by <sup>34</sup>S-depleted pyrite and preserved fatty acids
- Extensional events have facilitated deep microbial colonization

### Supporting Information:

Supporting Information may be found in the online version of this article.

### Correspondence to:

H. Drake,  
[henrik.drake@lnu.se](mailto:henrik.drake@lnu.se)

### Citation:

Drake, H., Makahnouk, W. R. M., Roberts, N. M. W., Reinhardt, M., Henkemans, E., Frapé, S. K., et al. (2024). Late Cretaceous and Early Paleogene fluid circulation and microbial activity in deep fracture networks of the Precambrian basement of Western Greenland. *Geochemistry, Geophysics, Geosystems*, 25, e2024GC011646. <https://doi.org/10.1029/2024GC011646>

Received 1 MAY 2024

Accepted 8 JUL 2024





### Author Contributions:

**Conceptualization:** H. Drake, W. R. M. Makahnouk  
**Data curation:** H. Drake, N. M. W. Roberts, M. J. Whitehouse  
**Formal analysis:** H. Drake, W. R. M. Makahnouk, N. M. W. Roberts, M. Reinhardt, C. Broman, M. J. Whitehouse, E. Kooijman  
**Funding acquisition:** H. Drake  
**Investigation:** H. Drake, W. R. M. Makahnouk, M. Reinhardt, E. Henkemans, S. K. Frapé, E.-L. Tullborg  
**Methodology:** H. Drake, W. R. M. Makahnouk, N. M. W. Roberts, M. Reinhardt, M. J. Whitehouse, E. Kooijman

© 2024 The Author(s). Geochemistry, Geophysics, Geosystems published by Wiley Periodicals LLC on behalf of American Geophysical Union.

This is an open access article under the terms of the [Creative Commons Attribution License](https://creativecommons.org/licenses/by/4.0/), which permits use, distribution and reproduction in any medium, provided the original work is properly cited.

## Late Cretaceous and Early Paleogene Fluid Circulation and Microbial Activity in Deep Fracture Networks of the Precambrian Basement of Western Greenland

H. Drake<sup>1</sup> , W. R. M. Makahnouk<sup>2</sup> , N. M. W. Roberts<sup>3</sup> , M. Reinhardt<sup>4</sup> , E. Henkemans<sup>2,5</sup>, S. K. Frapé<sup>2</sup>, E.-L. Tullborg<sup>6</sup>, C. Broman<sup>7</sup>, M. J. Whitehouse<sup>8</sup>, and E. Kooijman<sup>8</sup>

<sup>1</sup>Department of Biology and Environmental Science, Linnaeus University, Kalmar, Sweden, <sup>2</sup>Department of Earth & Environmental Sciences, University of Waterloo, Waterloo, ON, Canada, <sup>3</sup>Geochronology and Tracers Facility, British Geological Survey, Nottingham, UK, <sup>4</sup>Department of Geobiology, Geoscience Centre, University of Göttingen, Göttingen, Germany, <sup>5</sup>WSP Canada Inc., Whitehorse, YT, Canada, <sup>6</sup>Terralogica AB, Gråbo, Sweden, <sup>7</sup>Department of Geological Sciences, Stockholm University, Stockholm, Sweden, <sup>8</sup>Swedish Museum of Natural History, Stockholm, Sweden

**Abstract** Deep fracture-hosted fluids of Precambrian bedrock cratons are relatively stagnant over long time spans compared to near-surface systems. However, episodic events, such as fracture reactivations, transgressions, and deglaciations, may introduce dilute water, replacing, and mixing with the deep continental brines, thereby sparking microbial activity. Secondary minerals that line bedrock fractures serve as important geochemical archives for such episodic events. Here we explore the fracture mineral record of Archean rocks of Western Greenland by analyzing samples from deep boreholes with the aim to trace and characterize episodic paleofluid flow and paleomicrobial activity. A sequence of hydrothermal to low temperature fluid flow events is demonstrated. For the youngest generation, microscale S-isotope analysis of pyrite reveals substantial <sup>34</sup>S-depletion (minimum  $\delta^{34}\text{S}$ :  $-58\text{‰}$ -CDT) compared to fracture-hosted barite ( $\delta^{34}\text{S}$ :  $13\text{‰} \pm 2\text{‰}$ ) and gypsum ( $\delta^{34}\text{S}$ :  $2.6\text{‰}$ - $10.6\text{‰}$ ). This suggests the formation of pyrite following S isotope fractionation during microbial sulfate reduction. This metabolism is further indicated by several methyl-branched fatty acids preserved in calcite. A general discrepancy between calcite and groundwater  $\delta^{18}\text{O}$ -values suggests that calcite formed from water different from the presently residing glacial meltwater-influenced groundwater mix. High spatial resolution U-Pb carbonate geochronology of the youngest generation of calcite yielded ages for two samples:  $64 \pm 3$ ,  $75 \pm 7$  Ma ( $2\sigma$ ). These ages overlap with tectonic events related to early stages, or prestages, of the opening of the Atlantic and Labrador Seas. This suggests that deep fracture networks in Western Greenland were colonized by microorganisms, such as sulfate reducers, in the course of this extensional event.

## 1. Introduction

Deep fracture waters of Precambrian bedrock cratons are considered as relatively stagnant over long time spans compared to near-surface systems (Gimeno et al., 2023; Holland et al., 2013; Kietäväinen et al., 2014). Episodic events, such as fracture reactivation, transgressions, and deglaciations, can disrupt the prevailing conditions by introducing water of different compositions, for example, dilute glacial water that mixes with residing brines (Gómez et al., 2014). If ambient conditions stabilize, microbial blooms may result from infiltration of surficial microbial taxa (Westmeijer et al., 2022) fueled by substrates in the form of dissolved organic carbon (Hubalek et al., 2016; Osterholz et al., 2022) and by emerging geochemical gradients (Pedersen et al., 2014). Such events may induce mineral oversaturation with resultant mineral precipitation on fracture walls (Drake, Åström, et al., 2015; Sahlstedt et al., 2016). These minerals serve as important archives for past events of fracture reactivation, fluid circulation, and microbial activity, owing to the geochemical information they contain in the form of isotopic composition and trapped fluid inclusions (Drake, Heim, et al., 2017; Milodowski et al., 2018; Sandström & Tullborg, 2009; Tullborg et al., 1999, 2008). These mineral archives uncover discrete tectonic events within cratons and temporal variation in physicochemical conditions (e.g., temperatures and salinity) as well as habitable conditions for microbial colonization of the deep subsurface (Drake & Reiners, 2021).

In terms of paleohydrogeology in previously glaciated areas, there have been studies using fracture coating minerals in Finland (Blyth et al., 2002, 2004; Sahlstedt et al., 2010; Seitsamo-Ryynänen et al., 2022), Sweden (Drake, Ivarsson, et al., 2018; Tullborg et al., 1999, 2008), and the UK (Milodowski et al., 2018). These have seldom shown clear glacial meltwater-related mineral precipitates. There are also studies using a

**Project administration:** H. Drake  
**Resources:** H. Drake, S. K. Frapé  
**Software:** M. J. Whitehouse  
**Validation:** H. Drake,  
W. R. M. Makahnouk, M. J. Whitehouse,  
E. Kooijman  
**Visualization:** H. Drake,  
N. M. W. Roberts, M. Reinhardt  
**Writing – original draft:** H. Drake  
**Writing – review & editing:** H. Drake

paleohydrogeological approach based on groundwater chemistry of present-day waters (Gómez et al., 2014; Pitkänen et al., 2009; Stotler et al., 2009, 2012), showing that glacial components are clearly distinguishable in the fluid chemical signatures. To date, however, no paleohydrogeology investigations based on fracture coatings have been carried out in recently glaciated terrains. Consequently, little knowledge of potential mineralogical imprints caused by circulation of glacial meltwater and subpermafrost waters exists.

For the detection of biosignatures for ancient microbial activity, studies of Precambrian cratons have so far focused on the Fennoscandian shield, particularly in Sweden (Drake, Åström, et al., 2015; Drake, Heim, et al., 2017; Drake, Roberts, et al., 2021; Drake et al., 2023; Clauer et al., 1989; Sandström & Tullborg, 2009; Tullborg et al., 1999) and Finland (Sahlstedt et al., 2010, 2013, 2016). The dominance of Fennoscandian shield data in this field of research is related to extensive nuclear waste repository research in these countries, featuring deep drilling of cored boreholes. These studies investigated Paleoproterozoic (1.87–1.8 Ga) rocks and reported large ranges in  $\delta^{13}\text{C}$  values in calcite associated with microbial methane consumption and formation ( $-125\%$  to  $+37\%$ ),  $\delta^{34}\text{S}$  values in pyrite associated with microbial sulfate reduction (MSR,  $-54\%$  to  $+147\%$ ) (Blyth et al., 2000; Clauer et al., 1989; Drake, Åström, et al., 2015; Drake, Heim, et al., 2017; Drake, Roberts, et al., 2021; Sahlstedt et al., 2013, 2016; Tullborg et al., 1999), fossilized remnants of prokaryotes (Pedersen et al., 1997) and eukaryotes (Drake, Ivarsson, et al., 2021; Ivarsson, Broman, et al., 2013) as well as organic molecules of microbial origin (Drake, Åström, et al., 2015; Heim et al., 2012). Although not belonging to a Precambrian craton, fracture coatings in the Toki granite in Japan have also shown signals of methane oxidation, tracked by C isotope measurements of calcite (Mizuno et al., 2023). Geochronology investigations from the Fennoscandian shield show that mineral coatings with biosignatures have formed in the Phanerozoic at intervals 410–360, 160–170, 80–13 Ma (Drake, Heim, et al., 2017; Drake, Whitehouse, et al., 2018; Drake et al., 2019; Drake, Roberts, et al., 2021; Ivarsson et al., 2020; Tillberg et al., 2019), that coincide with thermochronology models showing crustal habitability at these times (Drake & Reiners, 2021). Biosignatures have also been detected in veins and vugs of oceanic crust, both in international oceanic drilling campaigns (Bengtson et al., 2014; Ivarsson, Bengtson, et al., 2013; Ivarsson et al., 2015), and in ophiolites (Carlsson et al., 2019; Ivarsson et al., 2019; Lima-Zaloumis et al., 2022), as well as in impact craters (Drake et al., 2019; Parnell et al., 2010; Simpson et al., 2017). Since studies of biosignatures of ancient life in fracture networks of Precambrian basement rocks outside of the Fennoscandian shield are scarce, there is little knowledge of how widespread signs of ancient life are in the vast ecosystem that the continental Precambrian crust represents.

Here we explore the fracture mineral record of Archean rocks by analyzing drill cores from boreholes near the margin of the continental ice sheet of Western Greenland. The investigations aim at gaining knowledge of paleofluid circulation and of potential paleomicrobiological signatures in the Precambrian craton, which is still unexplored in this context. The data set includes (a) high spatial resolution S isotope analysis of pyrite crystals, (b) C, O and Sr isotope analysis of calcite crystals, (c) S and O analysis of barite crystals, (d) conventional bulk sample analysis of C, O, Sr in calcite, (e) molecular analysis of calcite-trapped organic compounds, (f) fluid inclusion microthermometry analysis of calcite crystals, and (g) high spatial resolution U-Pb carbonate geochronology. We compare the results with hydrochemical data of fracture waters from the same borehole sections (Harper et al., 2016) to distinguish modern precipitates, particularly of glacial origin, in a cryogenic subsurface environment. This study also provides additional information on the neotectonic evolution of Western Greenland and on the opening of the North Atlantic, connecting to recent works on calcite veins linked to the opening of the Atlantic, for example, on the Faroe Islands (Roberts & Walker, 2016).

## 2. Geological Setting, Hydrogeology, Microbiology

The Kangerlussuaq area in central west Greenland is in an ice-free coastal zone. Barren bedrock ridges and stream valleys trending E-NE to W-SW dominate the landscape in front of the ice sheet. The stream valleys are sub-parallel to the ice movement and provide drainage to the fjords. The highest bedrock ridges close to the ice margin are about 600 m above sea level (m.a.s.l.). The area of the deep boreholes is located between the glacial outlets of Russel's Glacier to the south and Isunnguata Sermia to the north (Figure 1).

Three boreholes, GAP01, GAP03, and GAP04, were drilled within a joint project between the spent nuclear fuel management organizations of Sweden (SKB), Finland (Posiva) and Canada (NWMO). Details about the drilling and mapping of the drill cores, as well as about hydrological investigations are reported elsewhere (Liljedahl et al., 2021; Pere, 2014). Borehole GAP01 is 222 m long (191 m of vertical depth, ground surface elevation 374 m.

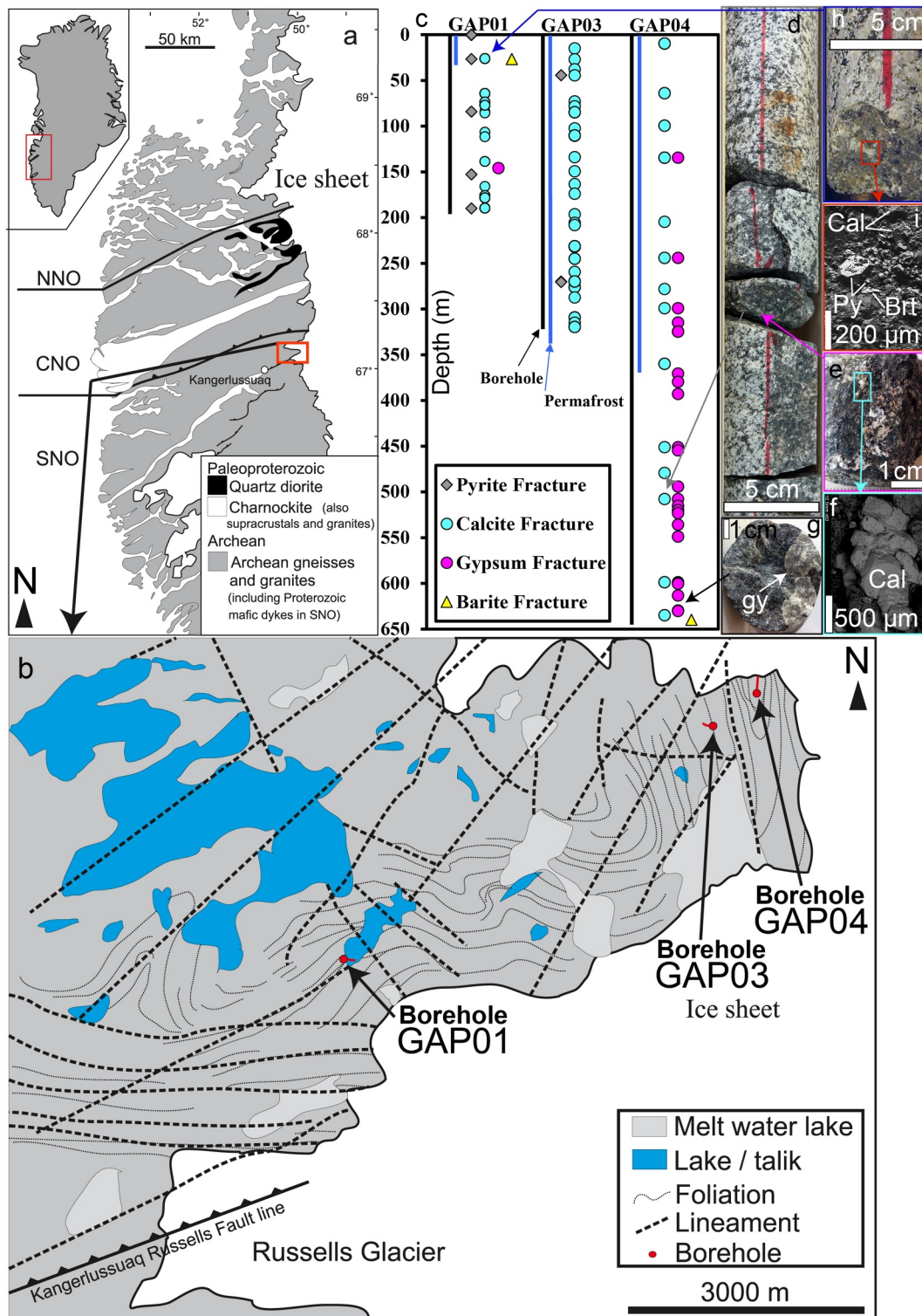


**Figure 1.** (a) Regional geological map of the Kangerlussuaq area in central Western Greenland. The study area is indicated by the red box next to Kangerlussuaq (Map modified from Garde & Hollis, 2010; Garde & Marker, 2010). Abbreviations segment of the Nagssugtoqidian Orogen, CNO, NNO = Southern, Central and Northern parts of the Nagssugtoqidian Orogen, respectively. (b) Close up map of the study area with foliation and lineaments shown (modified from Drake, Suksi, et al., 2017), with geological information from Engström and Klint (2014), as well as meltwater lakes and talik lakes. (c) Observations of fracture coating pyrite, calcite, gypsum and barite in boreholes, GAP01, 03, and 04, with depth extension of borehole and permafrost indicated. (d–i) Drill core photos, with close up of fracture surface for (d–f) Sample GAP04:550, with fracture-coating calcite (close-up in back-scattered scanning electron microscope [BSE-SEM] image in f), (g) GAP04:670, with fracture-coating gypsum, (h–i): GAP01:30 with fracture-coating barite, calcite, and pyrite (close-up in BSE-SEM image in i).



a.s.l.), and drilled 20 m from the shoreline of a lake, about 1 km from the ice margin. The GAP03 borehole (ground surface elevation 484 m.a.s.l.) was drilled to 341 m length (320 m of vertical depth), about 1 km from Isunnguata Sermia, 6 km NE from GAP01. The GAP04 drilling site, at 525 m.a.s.l., was located 200 m from the margin of the Isunnguata Sermia. This is the deepest of the boreholes, length: 687 m, vertical depth: 650 m, with a dip of 70° extending beneath the ice sheet.

## 2.1. Geology

### 2.1.1. Bedrock Geology

The study area is part of the southern segment of the Nagssugtoqidian Orogen (SNO) of West Greenland (Engström & Klint, 2014). Archean orthogneisses and a few paragneisses, having formation ages from ~2.85 to 2.70 Ga, occur across the orogen (Escher et al., 1976; Marker et al., 1995). The SNO includes granulite facies Archean gneisses and granitoids (tonalitic to granodioritic), intruded by a swarm of 2.04 Ga Paleoproterozoic mafic dykes (Cadman et al., 2001; Connolly, 1997; Noe-Nygaard & Ramberg, 1961; Nutman et al., 1999). All these rocks underwent amphibolite grade metamorphism during the Nagssugtoqidian orogeny, at 2.0–1.75 Ga (Escher et al., 1975, 1976). Since the Late Mesozoic, West Greenland has been a part of a passive margin east of the Davis Strait (Chalmers & Pulvertaft, 2001) with cross-cutting fracture sets that suggest relation to stress fields that governed the opening of the Labrador Sea-Davis Strait-Baffin Bay seaway (Wilson et al., 2006). This regional 50–100 Ma faulting related to seafloor spreading during the opening of the Labrador Sea and Baffin Bay is associated with NNE-SSW sinistral strike-slip faulting and conjugate dextral strike slip faulting. The event is locally attested by a sinistral strike-slip fault trending NE-SW, by reactivation of NE-SW trending pegmatites, as well as by a later set of dextral strike slip faults trending N-S (Engström & Klint, 2014). The mountains in West Greenland were formed by Cenozoic uplift and erosion (Bonow et al., 2006; Japsen et al., 2006). The bedrock structures in the Kangerlussuaq area include macroscale folds, gneissic fabric, evidence of shearing, and prominent lineaments such as the Kangerlussuaq-Russell thrust fault (Engström & Klint, 2014). Four to five distinguishable fracture sets occur in the area, of which the dominant is the foliation parallel, ENE-WSW (Klint et al., 2013; Wilson et al., 2006). There is no thermochronological evidence of thermal activity during Cenozoic times, suggesting that the thermal effects of Paleogene rifting and break-up were negligible and that the magnitude of Cenozoic erosion was <3.5 km in the Kangerlussuaq area (Danišik & Kirkland, 2023; Jess et al., 2018).

### 2.1.2. Bedrock Geology in Boreholes

The boreholes GAP01 and GAP03 are dominated by feldspar-rich felsic gneisses with interspersed sections of mafic and intermediate gneisses, whereas GAP04 has more of the latter (Pere, 2014). The boreholes intersect different parts of large folds, and the geometry of foliation and fracturing is therefore different. The foliation in GAP01 is striking predominantly NE-SW, with a steep dip toward the NW. The foliation in GAP03 strikes NNW-SSE, with a steep dip toward the NNE, whereas GAP04 was drilled in an open fold with a NNW-trending and shallowly plunging (~14°) synform (Engström & Klint, 2014). According to the drill core mapping (Pere, 2014), GAP01 is unevenly fractured, has scattered narrow highly fractured zones and an average fracture frequency of two fractures per meter (mainly steeply dipping). The main fracture filling minerals are calcite, chlorite and clay minerals (e.g., kaolinite). Pyrite, hematite, quartz, biotite, gypsum and feldspar occur sporadically. The average fracture frequency in GAP03 is 4 fractures per meter (mainly steeply dipping). The main fracture filling minerals are calcite, chlorite and clay minerals. Epidote, pyrite, biotite, quartz, chalcocopyrite, goethite and hematite occur sporadically. Drill core GAP04 has an average fracture frequency of 1.7 fractures per meter, with increased fracturing at around 500–600 m borehole length. Vertical fractures are common in the upper 300 m and sub-horizontal fractures dominate below 300 m. The main fracture minerals are chlorite, gypsum, calcite and clay. Pyrite, pyrrotite, Fe-oxyhydroxide and kaolinite are accessory phases.

## 2.2. Hydrology and Permafrost

Kangerlussuaq is located in a permafrost area (Brown et al., 1998), with unfrozen ground confined to localized thawed zones or taliks beneath lakes and rivers (French, 2007). The permafrost acts as an impermeable confining layer, which inhibits and re-directs groundwater flow and recharge. Subglacial permafrost in the borehole GAP04 evidences re-advance of the ice sheet over frozen ground (Ruskeeniemi et al., 2018). Borehole GAP01 is drilled

next to a lake and temperature profiling in the borehole shows that there is a talik below the lake (Harper et al., 2016). Modeling shows that presently there is minor recharge of lake water to the talik (Johansson et al., 2015).

Temperature profiling indicates that the permafrost thickness is about 350 m in GAP04 and 335 m in GAP03 (modeled thickness, base of permafrost is deeper than the borehole). Downhole monitoring of GAP04 shows that the hydraulic head varies over multi-annual, seasonal and diurnal timescales, possibly as a response to fluid pressure forcing at the ice/bed interface associated with changes in overlying ice loading and ice sheet hydrology (Liljedahl et al., 2021).

### 2.2.1. Deep Groundwater Beneath the Permafrost

Hydraulic testing of borehole GAP04 revealed sub-horizontal water conducting fracture zones with single or closely spaced fractures, below the permafrost, with highest transmissivities in a section between 548 and 604 m borehole length (Pöllänen et al., 2012). Sulfate and calcium concentrations in the deep groundwater sampled from GAP04 are high, c. 2,000 mg/L  $\text{SO}_4^{2-}$  and 660 mg/L  $\text{Ca}^{2+}$  in the deepest section (Harper et al., 2016), likely due to dissolution of gypsum fracture coatings. This groundwater shows low  $\delta^{18}\text{O}$  values,  $-23\text{‰}$  V-SMOW (Harper et al., 2016), indicating glacial meltwater origin. Similar strontium isotope ratios and  $\delta^{34}\text{S}$  and  $\delta^{18}\text{O}$  in sulfate from GAP04 and GAP01 waters and crush and leach derived waters indicate that the groundwater beneath the permafrost in GAP04 is recharged dilute meltwater that has evolved along the flow path to a Na-Ca- $\text{SO}_4$  water with total dissolved solids of  $\sim 3,000$  mg/L (Claesson Liljedahl et al., 2016; Henkemans, 2016; Henkemans et al., 2018). This suggests that the source of salinity in the groundwater is water-rock interaction with dissolution of gypsum as a major sulfate source.

### 2.2.2. Redox Fronts

Mineral coatings sampled from open fractures in drill cores from GAP01, 03, and 04 (down to 650 m; within and below the current permafrost) have been analyzed for redox histories (Drake, Suksi, et al., 2017). Disequilibrium in the  $^{238}\text{U}$ - $^{234}\text{U}$ - $^{230}\text{Th}$  system reveals the occurrence of redox related processes due to water circulation in the fracture system at various occasions during the last 1 Ma. In fractures of the upper 60 m, infiltration of oxygenated surface water has resulted in a prominent near-surface oxidized zone with abundant FeOOH precipitation. This zone must be a relict as it is located within current permafrost, and U deposition found within and below this zone indicates temporal redox variation within this zone during the last 1 Ma. Potential Holocene leaching of U is indicated by  $^{230}\text{Th}/^{238}\text{U} \gg 1$  in some of the near surface fractures and in a couple of deeper fractures. These observations are in line with documented movements of the ice front during the Holocene.

### 2.3. Microbiology

Microbiology investigations of the GAP borehole groundwater have aimed at determining the composition and estimating the metabolic features of the microbial communities (Bomberg et al., 2019). Bacteria 16S rRNA gene copies were  $< 1 \times 10^6 \text{ mL}^{-1}$ . Sulfur/iron reducing *Desulfosporosinus* sp. dominated the deep anaerobic groundwater (Bomberg et al., 2019), whereas archaea were almost undetectable ( $< 1\%$ ). The bacterial community of the deep groundwater consisted mostly of Firmicutes. The *Desulfosporosinus* genus had the highest relative abundance, and these sulfate reducers have the capacity to reduce Fe(III), nitrate, elemental sulfur and thiosulfate (Sánchez-Andrea et al., 2015). The other significant firmicutes group belongs to the SRB2 cluster of the Thermoanaerobacterales family (Bomberg et al., 2019). The latter are probably also sulfate reducers but have a broad range of possible electron donors and may even turn to fermentation in the absence of reducible electron acceptors (Sánchez-Andrea et al., 2015).

## 3. Methods

### 3.1. Samples and Sample Preparations

The cored boreholes were drilled in 2009 (GAP01, 03; 39 mm core diameter) and in 2011 (GAP04; 50.5 mm). Fracture coating samples were collected from the drill cores and focused on calcite-, pyrite-, and barite-bearing open fractures.

## 3.2. Analytical Methods

### 3.2.1. Secondary Ion Mass Spectrometry (SIMS)

Following sample characterization and mineral identification, which was carried out directly on the uncoated fracture surfaces using a Hitachi S-3400N SEM equipped with an integrated energy dispersive spectroscopy system under low-vacuum conditions, calcite, barite and pyrite crystals were handpicked and mounted in epoxy, polished to expose crystal cross-section and examined with SEM to document zonation. SIMS-analysis (10  $\mu\text{m}$  lateral beam dimension, 1–2  $\mu\text{m}$  depth dimension) of carbon, oxygen and sulfur isotopes were performed on a CAMECA IMS1280 Secondary Ion Mass Spectrometry (SIMS) at NordSIMS, Swedish Museum of Natural History, Sweden.

#### 3.2.1.1. Calcite

Analytical transects of up to 10 analyses were made within the crystals. In total, 567 analyses were conducted in calcite for  $\delta^{13}\text{C}$  (262) and  $\delta^{18}\text{O}$  (305). The settings follow those described in Drake, Åström, et al. (2015). The influence of organic matter and inclusions of other minerals was avoided by careful spot placement in areas in the crystals without micro-fractures or inclusions. The uncertainty associated with potential organic inclusions and matrix composition is therefore considered insignificant compared to the isotope variations.

Calcite results are reported as ‰  $\delta^{13}\text{C}$  and  $\delta^{18}\text{O}$  based on the Pee Dee Belemnite (V-PDB)-standard value. Analytical sessions were carried out using running blocks of six unknowns bracketed by two standards. Spot transects were made from core to rim within the crystals (full data in Table S1 in Supporting Information S1). Corresponding analytical spots for C and O isotopes were closely placed within the crystals and analyzed in separate sessions. Isotope data were normalized using calcite reference material S0161, which comes from granulite facies marble in the Adirondack Mountains, courtesy of R.A. Stern (University of Alberta). The values used for IMF correction were determined by conventional stable isotope mass spectrometry at Stockholm University on 10 separate pieces, yielding  $\delta^{13}\text{C} = -0.22\text{‰} \pm 0.11\text{‰V-PDB}$  (1 std. dev.) and  $\delta^{18}\text{O} = -5.62\text{‰} \pm 0.11\text{‰V-PDB}$  (1 std. dev., Table S2 in Supporting Information S1). Precision was  $\delta^{18}\text{O}:\pm 0.2\text{‰}-0.3\text{‰}$  and  $\delta^{13}\text{C}:\pm 0.4\text{‰}-0.5\text{‰}$ .

#### 3.2.1.2. Barite

Three and five crystals were analyzed from the two samples GAP04:681 and GAP01:30, respectively, and two to six analyses were done on each crystal in transects, with closely spaced analyses for  $\delta^{34}\text{S}$  and  $\delta^{18}\text{O}$ . A total of 24 analyses for  $\delta^{18}\text{O}$  and 19 for  $\delta^{34}\text{S}$  were performed (Table S3 in Supporting Information S1). Separate analytical routines applied for S and O are described briefly below, and closely follow those described by Whitehouse (2013) for sulfur, with the exception that only  $^{34}\text{S}/^{32}\text{S}$  was measured here, and Heinonen et al. (2015) for oxygen. For both elements, the samples were sputtered using a Gaussian focussed  $^{133}\text{Cs}^+$  primary beam with 20 kV incident energy (10 kV primary, –10 kV secondary) and primary beam current of  $\sim 3$  nA, which was rastered over a  $5 \times 5$   $\mu\text{m}$  area during analysis to homogenize the beam density. A normal incidence electron gun was used for charge compensation. Analyses were performed in automated sequences, with each analysis comprising a 40-s pre-sputter to remove the gold coating over a rastered  $15 \times 15$   $\mu\text{m}$  area, centering of the secondary beam in the field aperture to correct for small variations in surface relief, and data acquisition in twelve four-second integration cycles. The magnetic field was locked at the beginning of the session using an NMR field sensor. Secondary ion signals ( $^{32}\text{S}$  and  $^{34}\text{S}$  or  $^{16}\text{O}$  and  $^{18}\text{O}$ ) were detected simultaneously using two Faraday detectors with a common mass resolution of 4,860 ( $M/\Delta M$ ) for S and 2,430 ( $M/\Delta M$ ) for O. Data were normalized for instrumental mass fractionation using matrix-matched reference materials mounted in the sample mounts and analyzed after every sixth sample analysis. The S0327 reference material, with a conventionally determined  $\delta^{34}\text{S}$  value of  $22.0\text{‰} \pm 0.3\text{‰}$  and  $\delta^{18}\text{O}$  value of  $11.0\text{‰} \pm 0.1\text{‰}$  (Liseroudi Mastaneh et al., 2021) was used (Table S4 in Supporting Information S1). Typical precision on a single  $\delta^{34}\text{S}$  and  $\delta^{18}\text{O}$  value, after propagating the within run and external uncertainties from the standard measurements was  $\pm 0.2\text{‰}$  ( $1\sigma$ ) and  $0.23\text{‰}$  ( $1\sigma$ ), respectively. All results are reported with respect to the V-CDT (Ding et al., 2001) and V-SMOW (Coplen, 1995) for oxygen.

#### 3.2.1.3. Pyrite

Sulfur was sputtered using a  $^{133}\text{Cs}^+$  primary beam with 20 kV incident energy (10 kV primary, –10 kV secondary) and a primary beam current of  $\sim 1.5$  nA. A normal incidence electron gun was used for charge

compensation. Analyses were performed in automated sequences, with each analysis comprising a 70 s pre-sputter to remove the gold coating over a rastered  $15 \times 15 \mu\text{m}$  area, centering of the secondary beam in the field aperture to correct for small variations in surface relief and data acquisition in 16 four second integration cycles. The magnetic field was locked at the beginning of the session using an NMR field sensor. Secondary ion signals for  $^{32}\text{S}$  and  $^{34}\text{S}$  were detected simultaneously using two F detectors with a common mass resolution of 4,860 ( $M/\Delta M$ ). Results,  $n = 126$ , are reported as ‰  $\delta^{34}\text{S}$  based on the Canon Diablo Troilite (V-CDT)-standard value (Ding et al., 2001). Analytical transects of up to 11 spots were made from core to rim in the crystals (data listed in Table S5, reference materials in Table S6 in Supporting Information S1). One to seven crystals were analyzed from each sample. The reference material for one session was the Ruttan pyrite that has conventionally determined values of  $+1.408\text{‰}$  (Cabral et al., 2013). For the other sessions, the pyrite reference material S0302A with a conventionally determined value of  $0.0\text{‰} \pm 0.2\text{‰}$  (R. Stern, University of Alberta, pers. comm.) was used. Typical precision on a single  $\delta^{34}\text{S}$  value, after propagating the within run (typically  $<0.1\text{‰}$ ) and external uncertainties from the standard measurements was  $\pm 0.14\text{‰}$  for pyrite ( $\pm 0.09\text{‰}$  for the S0302A session).

### 3.2.2. LA-MC-ICP-MS, $^{87}\text{Sr}/^{86}\text{Sr}$ Calcite

Analysis of  $^{87}\text{Sr}/^{86}\text{Sr}$  in calcite ( $n = 46$ , Table S1 in Supporting Information S1) was conducted by laser ablation multi-collector inductively coupled plasma mass spectrometry (LA-MC-ICP-MS) analysis at the Vegacenter, Swedish Museum of Natural History, Stockholm, Sweden, using a Nu plasma (II) MC-ICP-MS and an ESI NWR193 ArF excimer laser ablation (15 Hz) system following methods presented in Drake et al. (2020). The spot size was  $80 \mu\text{m}$ , fluence  $2.7 \text{ J/cm}^2$ , with washout and ablation times of 40 and 45 s, respectively. All measurements of  $^{87}\text{Sr}/^{86}\text{Sr}$  were normalized to an in-house brachiopod reference material “*Encomiosa gerda*” (linear drift and accuracy correction) using a value established by TIMS of 0.709168 (2sd 0.000004) (Kiel et al., 2014). A secondary reference material—a modern oyster shell from Western Australia—was analyzed at regular intervals along with the primary reference. Comparison to the modern seawater value for  $^{87}\text{Sr}/^{86}\text{Sr}$  of  $0.7091792 \pm 0.0000021$  (Mokadem et al., 2015) was used to quantify the accuracy of these analyses (Table S7 in Supporting Information S1).

### 3.2.3. Conventional Isotope Analysis

For calcite, conventional bulk sample  $\delta^{13}\text{C}$  and  $\delta^{18}\text{O}$  analysis was performed for 64 calcite aliquots (Table S8 in Supporting Information S1, including a few with co-genetic dolomite). For  $^{87}\text{Sr}/^{86}\text{Sr}$ , the total number of analyses was 40 (Table S8 in Supporting Information S1). Small sections of calcite mineralogy were carefully sampled from fractures with the aid of a binocular microscope and dental tools. In cases where multiple generations were evident in fractures, small chips of calcite were removed from different layers of fracture infilling material. Carbonate samples were then ground to a fine powder with an agate mortar and pestle to homogenize the sample.

Isotope analyses for  $\delta^{13}\text{C}$  and  $\delta^{18}\text{O}$  were completed by the Environmental Isotope Laboratory at the University of Waterloo (EIL-UW) and Isotope Tracer Technologies (IT<sup>2</sup>) to have inter-laboratory comparisons of results. Small aliquots of calcite and dolomite powders ( $\sim 0.25 \text{ mg}$  of powder) were weighed for each sample and the sample vials were purged with continuous He gas flow to remove atmospheric  $\text{CO}_2$ . Mass analysis was conducted by reacting calcite and dolomite with 100% orthophosphoric acid ( $\text{H}_3\text{PO}_4$ ) at  $90^\circ\text{C}$  and  $50^\circ\text{C}$  (EIL-UW and IT<sup>2</sup>, respectively) to generate  $\text{CO}_2$  gas, similar to established techniques (Al-Aasm et al., 1990; Paul & Skrzypek, 2007). Isotopic measurements of  $\text{CO}_2$  gas were conducted using a GV Instruments Isoprime and Trace Gas gas chromatograph (GC) Interface coupled with Gilson 222 XL Liquid Handler and autosampler for sample introduction (EIL-UW) and ThermoFinnigan EA 1110 (IT<sup>2</sup>) instrument using manual sample injection. Isotopic results were reported in  $\delta$  notation, expressed in parts per thousand (per mil, ‰) with respect to V-PDB.

$$\delta = \frac{R_{\text{sample}} - R_{\text{std}}}{R_{\text{std}}} \times 1,000$$

Standard Reference Materials used in this study for data correction were calcite standards: NBS-19 ( $\delta^{13}\text{C} = +1.95\text{‰}$ ,  $\delta^{18}\text{O} = -2.20\text{‰}$ ), IAEA CO-8 ( $\delta^{13}\text{C} = -5.76\text{‰}$ ,  $\delta^{18}\text{O} = -22.70\text{‰}$ ), Tauber ( $\delta^{13}\text{C} = -25.87\text{‰}$ ,  $\delta^{18}\text{O} = -25.74\text{‰}$ ; Copenhagen, DK), and EIL-21 ( $\delta^{13}\text{C} = -0.19\text{‰}$ ,  $\delta^{18}\text{O} = -15.68\text{‰}$ ; EIL-UW Internal Standard, Pine Point NS). Reproducibility for the results for most analyses was better than  $\pm 0.2\text{‰}$  (Table S8 in Supporting Information S1).

Strontium was extracted from calcite using Eichrom strontium-specific resin composed of crown ethers. These crown ether structures have high affinity for Pb and Sr in nitric acid (Horwitz et al., 1992, 1994). The ions are then released from the resin using milli-Q deionized water, which makes it useful for Sr purification. The extraction method used in this study was developed based on resin binding data (Horwitz et al., 1992, 1994) and is similar to other studies (Andrews et al., 2016; Wang et al., 2019). A 1  $\mu\text{g}$  aliquot of strontium is loaded on the center of a rhenium filament following an established methodology (Di Salvo et al., 2018; Tuttas & Schwieters, 2008). Intensities of  $^{84}\text{Sr}$ ,  $^{86}\text{Sr}$ ,  $^{87}\text{Sr}$ , and  $^{88}\text{Sr}$  were measured by TIMS using the double rhenium filament technique. During data collection,  $^{85}\text{Rb}$  was monitored to ensure there was no isobaric  $^{87}\text{Rb}$  interference with  $^{87}\text{Sr}$ . Analyses are conducted using an ion beam for  $^{88}\text{Sr}$  with an intensity set at 1.5 V measuring 200 cycles with integration times of 8 and 4 s idle times. Results are obtained by normalizing  $^{87/86}\text{Sr}$  ratio relative to a value of 8.375209 for the  $^{88/86}\text{Sr}$  ratio. The  $^{87/86}\text{Sr}$  ratio was corrected using the NIST987 standard reference material ( $^{87/86}\text{Sr} = 0.710245$ ). With the TIMS instrumental set-up, the magazine in the source housing holds 21 samples, three NIST987 samples are analyzed throughout the analytical run and the precision of unknown analyses are reported by standard error that has been calculated using the variance of the three measurements for NIST987. Three duplicate samples of unknowns are also analyzed for reproducibility and precision. The current long-term  $^{87/86}\text{Sr}$  mean (2012–2024) for NIST987 is 0.710278 ( $2\sigma_{\text{SD}} = 0.000041$ ,  $n = 640$ ). External precision for  $^{87/86}\text{Sr}$  measurements is also evaluated using Pacific Ocean seawater (Cabo San Lucas). The mean of  $^{87/86}\text{Sr}$  (2019–2024) for this Pacific Ocean water is 0.709180 ( $2\sigma_{\text{SD}} = 0.000051$ ,  $n = 57$ ).

### 3.2.4. Fluid Inclusions

Fluid inclusion analysis was conducted using a Nikon microscope equipped with a Linkam THMS600 heating and freezing microscope stage at Stockholm University, Sweden, and University of Waterloo, Canada. The working range of the stage is from  $-196^\circ$  to  $+600^\circ\text{C}$  (Shepherd et al., 1985). Fluid inclusion measurements on small chips of double polished carbonate sections and on hand-picked mm-sized calcite fragments were performed using methods described by Roedder (1984). Double polished sections were prepared using a Duren ore polisher. Fluid inclusions were completely frozen by super-cooling using liquid nitrogen and initial melting runs were performed using a heating rate of  $5\text{--}10^\circ\text{C}/\text{min}$  to measure the first melting ( $T_e$ ) and final melting ( $T_m$ ) temperatures. Heating programs were created using Linkam software to change the rates during melting runs, slowing down the heating rates to  $1\text{--}2^\circ\text{C}/\text{min}$  near the initially observed  $T_e$  and  $T_m$  for more accurate observation of these temperatures. Several melting runs were conducted in order to ensure that meta-stable melting temperatures were not observed and that consistent temperatures were recorded. After cooling/melting runs were completed, the fluid inclusions were then heated at  $5\text{--}10^\circ\text{C}/\text{min}$  until the gas-phase vapor bubble homogenized with the liquid and the homogenization temperature ( $T_h$ ) was recorded. As with the melting runs, heating programs were created using Linkam software to change the rates during the homogenization runs, slowing down the heating rates to  $1\text{--}2^\circ\text{C}/\text{min}$  near the initially observed  $T_h$  for more accurate observation of these temperatures. A cycling technique that was described by Roedder (1984) was used to measure homogenization temperatures when it was challenging to observe when the vapor bubble disappeared in the fluid inclusion. Once the  $T_h$  was recorded, the double polished chip was not used for additional thermometric measurements to eliminate the possibility of stretching, which can occur when soft minerals are overheated (Roedder, 1984). In the Waterloo laboratory, calibration of the fluid inclusion stage was checked daily using synthetic  $\text{CO}_2$  and  $\text{H}_2\text{O}$  fluid inclusions. Precision was  $\pm 0.1^\circ\text{C}$  for melting temperatures ( $\text{CO}_2$ :  $-56.6^\circ\text{C}$ ;  $\text{H}_2\text{O}$ :  $0.0^\circ\text{C}$ ) and  $\pm 1^\circ\text{C}$  for the critical point of water ( $374.1^\circ\text{C}$ ). In the Stockholm laboratory, the thermocouple readings were calibrated by means of SynFlinC® synthetic fluid inclusions and well-defined natural inclusions in Alpine quartz. The reproducibility was  $\pm 0.1^\circ\text{C}$  for  $<40$  and  $\pm 0.5^\circ\text{C}$  for temperatures  $>40^\circ\text{C}$ .

Fluid inclusion  $T_m$  temperatures are used to estimate salinity (wt. % NaCl) using equations that calculate wt % total salt as a function of temperature (Oakes et al., 1990; Potter et al., 1978). Isotopic signatures of paleo-fluids (i.e.,  $\delta^{13}\text{C}_{\text{CO}_2}$  and  $\delta^{18}\text{O}_{\text{H}_2\text{O}}$ ) are calculated using the fluid inclusion  $T_h$  temperatures and fractionation factor—temperature equations for  $\text{CO}_2\text{--CaCO}_3$  (Bottinga, 1968) and  $\text{CaCO}_3\text{--H}_2\text{O}$  (O'Neil et al., 1969), respectively.

### 3.2.5. U-Pb Geochronology

U-Pb geochronology via the in situ LA-MC-ICP-MS method was conducted at the Geochronology & Tracers Facility, British Geological Survey (Nottingham, UK). The method utilizes a New Wave Research 193UC excimer laser ablation system coupled to a Nu Instruments Nu Plasma multi-collector ICP-MS. The method



follows that previously described in Roberts and Walker (2016) and involves a standard-sample bracketing with normalization to NIST 614 silicate glass for Pb-Pb ratios (values of Woodhead & Hergt, 2001) and WC-1 carbonate for U-Pb ratios (Roberts et al., 2017). The laser parameters comprise an 80  $\mu\text{m}$  static spot fired at 10 Hz, with a  $\sim 6 \text{ J/cm}^2$  fluence, for 30 s of ablation. Material is pre-ablated to clean the sample site with 120  $\mu\text{m}$  spots for 3 s. No common lead correction is made; ages are determined by Model 1 regression and the lower intercept on a Tera-Wasserburg plot (using IsoplotR; Vermeesch, 2018). Duff Brown, a carbonate previously measured by Isotope Dilution mass spectrometry, was used as a validation, and yielded ages of  $65.6 \pm 0.5$  and  $65.67 \pm 0.65$  Ma for the two sessions, overlapping the published age of  $64.04 \pm 0.67$  Ma (Hill et al., 2016). All ages are plotted and quoted at  $2\sigma$  and include propagation of overdispersion and systematic uncertainties according to the recommended guidelines of Horstwood et al. (2016). Data are screened for low Pb and U counts below detection. Five samples were screened; only two yielded robust U-Pb ages, and the three others (GAP04:559, GAP04:459, GAP04:601) did not yield any radiogenic data. The samples were measured on crystals that were previously used for in situ stable isotope analysis via SIMS. Full analytical data from the sessions are listed in Table S9 in Supporting Information S1 and analytical conditions in Table S10 in Supporting Information S1.

### 3.2.6. Biomarkers

Glass and metal tools used for organic-geochemical preparation were heat-cleaned, and organic solvents were distilled and checked with gas chromatography–mass spectrometry (GC-MS). First, 0.1 g of calcite (GAP01:30, GAP01:219, GAP03:287, GAP04:550) was extracted with methanol (MeOH), dichloromethane (DCM) and *n*-hexane (10 min ultrasonication, respectively). The extract was gently dried at 40°C under nitrogen and derivatized with trimethylchlorosilane/methanol (TMCS/MeOH, 1/9, v/v) at 35°C for 2h. The solvent extracted calcite was then crushed with a glass stick and dissolved with 1 mL TMCS/MeOH (1/9, v/v) over night. The resulting liquid was subsequently extracted with *n*-hexane, and the extract was chromatographically separated into a hydrocarbon, fatty acid methyl ester and polar fraction using a glass column with 7.5 cm height and 1.5 cm inner diameter (filled with 0.7 g silica gel). 7 mL *n*-hexane was used for hydrocarbon separation, 7 mL DCM for fatty acid methyl ester separation, and 10 mL DCM/MeOH (3/1, v/v) for the polar residue. The latter was derivatized with *N,O*-bis(trimethylsilyl)trifluoroacetamide at 80°C for 2h. The separated fractions, a fatty acid methyl ester standard mix and an eicosane- $\text{D}_{42}$  standard were analyzed with a Thermo Scientific trace 1,300 GC coupled to a Thermo TSQ Quantum Ultra triple quadrupole mass spectrometer (MS). The GC was equipped with a 30 m Phenomenex Zebtron ZB-5MS column (0.25  $\mu\text{m}$  film thickness and 0.32 mm inner diameter). Helium was used as the carrier gas (1.5 mL/min flow rate). The samples were injected in splitless mode, and the injector was heated to 300°C. The initial GC oven temperature was 80°C (held for 1 min). The temperature was raised to 310°C with 6°C/min (held for 30 min). The ion source temperature in the MS was 240°C. The ionization energy was 70 eV. The scan range was set between 50 and 600 amu.

## 4. Results

### 4.1. Mineralogy

Sampling focused on open fractures but also included some sealed fractures. The sealed fractures contained veins of calcite, quartz, chlorite, albite, illite, occasionally pyrite (up to mm-sized euhedral crystals, Figure S1 in Supporting Information S1) and dolomite. A few vein pyrites and calcites were analyzed for stable isotopes. The drill core mapping showed that calcite was frequent throughout all depths (Figure 1c) (Pere, 2014). Pyrite was rare in GAP01 and GAP03 and basically non-existing in GAP04. Gypsum occurred in GAP04 preferentially but not exclusively beneath the permafrost. Barite was not noted in the drill core mapping but was observed with SEM (Figures 1i and 2d). The gypsum coatings occurred as smooth thin layers on the fracture surface (Figure 1g), whereas calcite, pyrite and barite occurred as euhedral crystals (Figures 1i, 1f, and 2). In a few cases, such as in GAP01:30, barite, calcite and pyrite were in paragenesis (Figure 1i). There were also samples with intergrown gypsum and barite (e.g., GAP04:600.07, Figure S2 in Supporting Information S1). Other paragenetic minerals in the open fractures are celestine (intergrown with barite), chlorite, clay minerals, quartz, bastnäsite, and goethite (mostly near surface, cf. Drake, Suksi, et al., 2017).

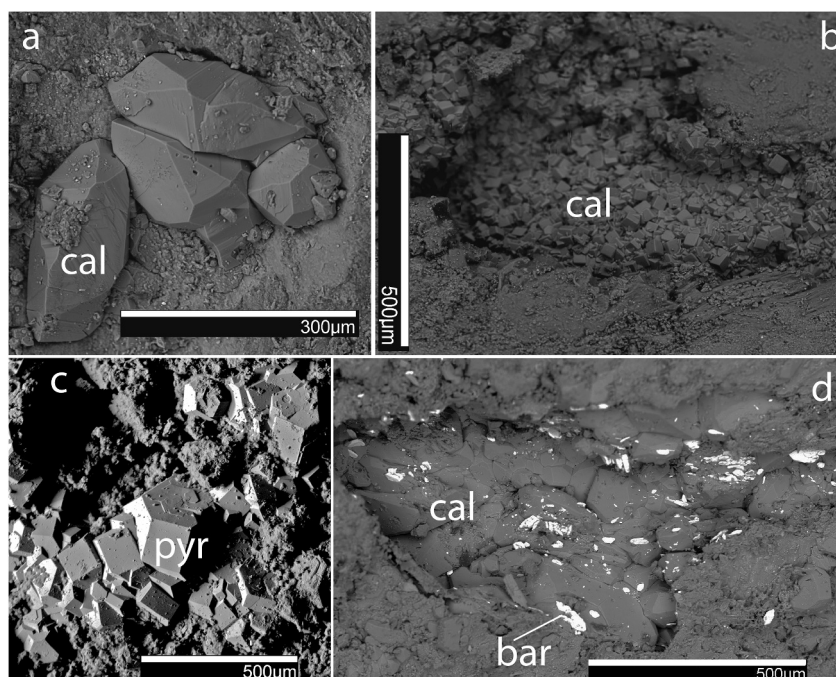


**Figure 2.** Mineral paragenesis and appearance. BSE-images of (a) Euhedral calcite (cal), partially with scalenohedral habit, on the fracture surface of sample GAP04:601.67. (b) Fine-grained aggregates of rhombohedral calcite in a vug of sample GAP04:637.07. (c) An aggregate of euhedral pyrite (pyr; cubic to pyritohedral), on the fracture surface of sample GAP01:209.60. (d) Fine-grained aggregates of equant calcite and bright barite (bar) crystals in a vug of sample GAP04:681.

## 4.2. Stable Isotopes

### 4.2.1. Calcite: $\delta^{13}\text{C}$ , $\delta^{18}\text{O}$ , $^{87}\text{Sr}/^{86}\text{Sr}$

Calcite was measured in bulk samples for C, O, and Sr isotopes, and in micro-scale using SIMS (C, O) and LA-MC-ICP-MS (Sr). The SIMS data showed average values of  $\delta^{13}\text{C}$ :  $-10.7\text{‰} \pm 3.0\text{‰}$  (1SD),  $\delta^{18}\text{O}$ :  $-15.1\text{‰} \pm 2.1\text{‰}$  and ranges of  $-25.1$  to  $-6.2$  and  $-21.7\text{‰}$  to  $-9.0\text{‰}$ , respectively. Bulk data showed average values of  $-8.9\text{‰} \pm 1.7\text{‰}$  and  $-14.7 \pm 1.7\text{‰}$  and ranges of  $-12.2$  to  $-5.0\text{‰}$  and  $-21.3$  to  $-10.0\text{‰}$ . The values do not show any distinct groups in a scatter plot of  $\delta^{13}\text{C}$  versus  $\delta^{18}\text{O}$  (Figure 3c), except for potentially two groups in  $\delta^{18}\text{O}$  (one dominant clustering around  $-15\text{‰}$  to  $-13\text{‰}$  V-PDB, and one less densely clustered with lower values,  $-21\text{‰}$  to  $-16.5\text{‰}$  range), and one outlier with low  $\delta^{13}\text{C}$ . The bulk sample values are relatively constant versus depth (Figure 3), and the micro-scale values are more varied on the sample scale as well as showing local  $\delta^{13}\text{C}$  depletions at  $\sim 90$  m and below 500 m (in GAP04). This discrepancy can be explained by the analytical scale, that is, the SIMS analyses were done on fine-grained euhedral crystals, whereas the bulk samples were scraped off from both euhedral crystals and older anhedral coatings underneath the euhedral crystals, representing a mixed signal.

For strontium,  $^{87}\text{Sr}/^{86}\text{Sr}_{\text{calcite}}$ , the highest values are in the upper 100 m (Figure 3d), mainly around 0.710–0.711, with some exceptions, and from these depths down to 350 m, there is a slight decline in  $^{87}\text{Sr}/^{86}\text{Sr}$  (from 0.709 to 0.706), although there is a large scatter. The deepest samples, from GAP04, beneath the permafrost, are generally lower in  $^{87}\text{Sr}/^{86}\text{Sr}$  (mean values of  $0.702 \pm 0.02$  to  $0.704 \pm 0.02$ ).

A few representative examples of the evolution of isotope values within individual calcite crystals are shown in Figure 4. Clear zonation is observed in some crystals, such as in GAP01:30 (Figure 4b), but the evolution from inner zones to outer rims is usually not straightforward. In the latter sample, the  $\delta^{13}\text{C}$  shows a dip of  $6\text{‰}$  in the center of the crystal, and the  $\delta^{18}\text{O}$  values show a clear increase from the inner zone (analyses #1 and #2) to the outer zones, whereas the  $^{87}\text{Sr}/^{86}\text{Sr}$  values are less consistent. Sample GAP04:550 (Figure 4c) shows much more consistency throughout the crystal, with a large inner growth zone (#1, #2) and a tiny first overgrowth (#3) that has more or less consistent values of  $\delta^{13}\text{C}$  ( $-15\text{‰} \pm 0.8\text{‰}$ ) and  $\delta^{18}\text{O}$  ( $-14\text{‰} \pm 0.6\text{‰}$ ). The outermost growth zone

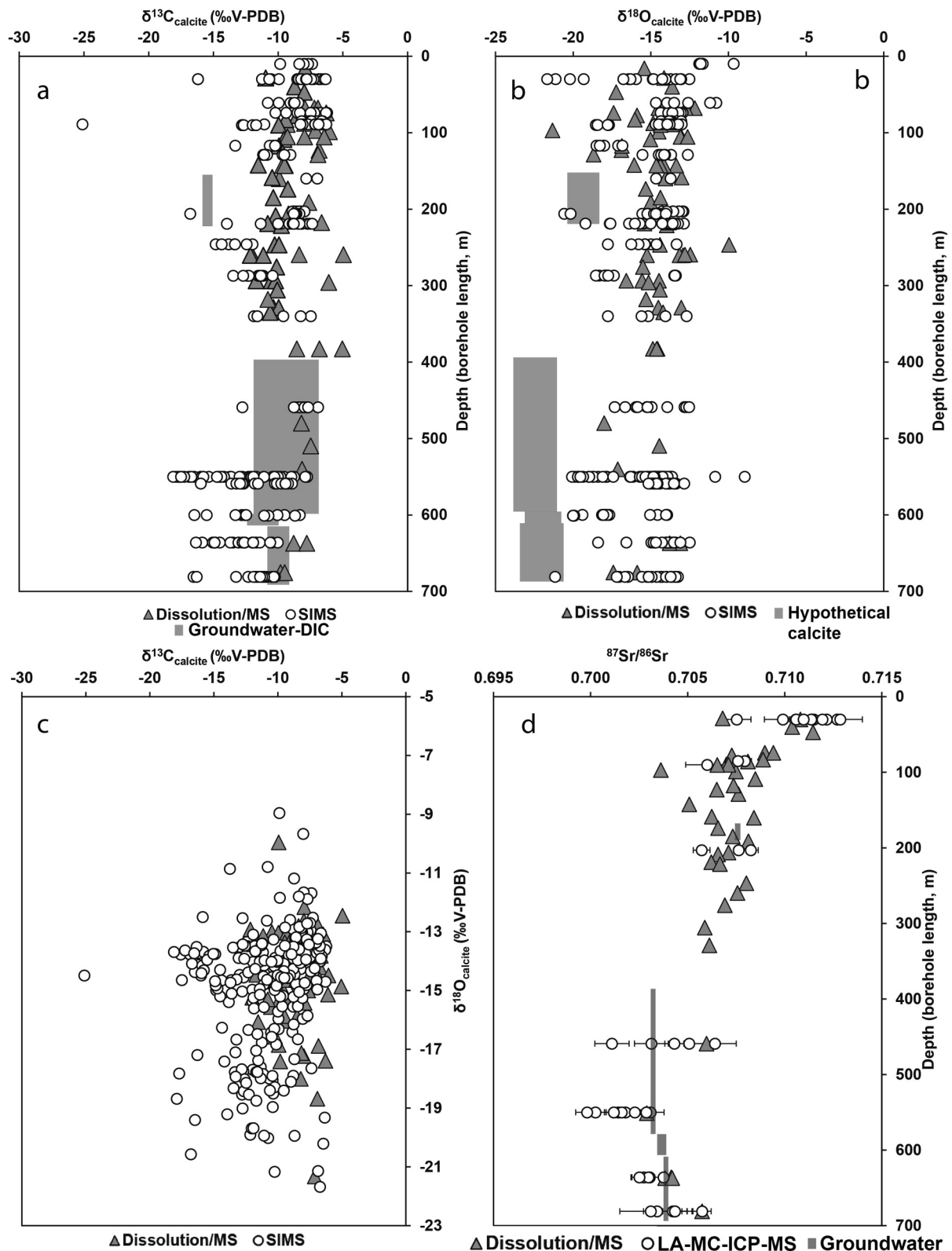


**Figure 3.** Stable isotope data of fracture-coated calcite, (a)  $\delta^{13}\text{C}$  versus depth, (b)  $\delta^{18}\text{O}$  versus depth, (c)  $\delta^{13}\text{C}$  versus  $\delta^{18}\text{O}$ , (d)  $^{87}\text{Sr}/^{86}\text{Sr}$  versus depth. Also included are groundwater data (from top two bottom): GAP01, GAP04: upper, middle, lower sections for  $\delta^{13}\text{C}$ -DIC (a), values for hypothetical modern calcite if precipitated from the current groundwater at 3–12°C (applying fractionation factors from Kim & O’Neil, 1997), correction for flushing water contamination (in GAP04: upper and middle) (b), and  $^{87}\text{Sr}/^{86}\text{Sr}$  (d).

has consistent  $\delta^{18}\text{O}$  but slightly elevated  $\delta^{13}\text{C}$  ( $-11.1\text{‰}$ ). The  $^{87}\text{Sr}/^{86}\text{Sr}$  values show small differences in the range 0.700–0.702. Sample GAP01:219 (Figure 4e) did not show any BSE-SEM indications of zonation, and the isotope values show variability of  $1\text{‰}$ – $2\text{‰}$  for  $\delta^{18}\text{O}$  or  $\delta^{13}\text{C}$  (Figure 4f). The samples beneath the permafrost in GAP04; GAP04:636 (Figures 4g and 4h) and GAP04:681 (Figures 4i and 4j) show a rather similar evolution, with low  $\delta^{18}\text{O}$  values in the inner zone ( $-17\text{‰}$  and  $-21\text{‰}$ , respectively) followed by higher values ( $-15 \pm 1\text{‰}$ ), whereas  $\delta^{13}\text{C}$  and  $^{87}\text{Sr}/^{86}\text{Sr}$  show a slightly more complex evolution with minor dips and spikes, albeit within a relatively minor range in values.

#### 4.2.2. Barite, $\delta^{18}\text{O}$ , $\delta^{34}\text{S}$

The two measured barite samples had similar  $\delta^{18}\text{O}$  composition ( $9.6 \pm 1.5\text{‰}$  and  $10.1 \pm 1.6\text{‰}$ ), but the deeper sample (GAP04:681) had lower  $\delta^{34}\text{S}$  values ( $6.9\text{‰} \pm 0.8\text{‰}$ ) than the shallower sample ( $13.0\text{‰} \pm 1.9\text{‰}$ , GAP01:30). Differences within the grains were relatively small, up to  $3\text{‰}$ – $4\text{‰}$  for both samples and isotope systems and did not show any obvious trends (Figure 5).

#### 4.2.3. Pyrite, $\delta^{34}\text{S}$

The six pyrite samples analyzed with SIMS group into two distinct groups. The first consists of relatively large pyrite grains (0.5–2 mm,  $n = 2$ ) in veins, which has homogeneous  $\delta^{34}\text{S}$  values close to  $0\text{‰}$  ( $0.3\text{‰} \pm 0.4\text{‰}$  V-CDT, sample GAP03:47) or slightly higher ( $4.2\text{‰} \pm 0.3\text{‰}$ , GAP01:97). A transect of homogeneous  $\delta^{34}\text{S}$  values throughout a crystal from GAP03:47 is shown in Figures 6a and 6b. The other group features smaller euhedral to subhedral crystals ( $n = 4$ ) and has much lower and more varied  $\delta^{34}\text{S}$  values ( $-59$  to  $-17\text{‰}$ ). All of these samples have minimum values below  $-39\text{‰}$ . The samples are relatively homogeneous in  $\delta^{34}\text{S}$  values, GAP01:30: spanning from  $-58.5$  to  $-51.2$  (average  $\pm$  st.dev =  $-55.1 \pm 2.0\text{‰}$ ), GAP01:176:  $-46.7$  to  $-34.3$  ( $-44.4 \pm 3.4\text{‰}$ ), GAP01:219:  $-54.9$  to  $-17.3\text{‰}$  ( $-39.6 \pm 10.7\text{‰}$ ) and GAP03:287:  $-39.4\text{‰}$  to  $-34.2\text{‰}$  ( $-36.4\text{‰} \pm 1.6\text{‰}$ ). The  $\delta^{34}\text{S}$  values of microscale analyses within individual crystals of these samples showed relatively small variation (Figure 6). The largest span within a crystal was  $7.2\text{‰}$  in GAP01:219.

#### 4.3. Fluid Inclusions

The inclusions were found to have a primary appearance (Roedder, 1984) and occur essentially as randomly distributed single fluid inclusions. The final melting is interpreted as ice melting and measured values yielded temperatures corresponding to salinity of 2.2–4.7 eq. mass % NaCl for sample GAP01:219, 0.18 for GAP01:74, between 1.9 and 11.6 for GAP03:47 and between 23.6 and 26.2 for GAP01:97 (dolomite) for the  $\text{CaCl}_2$ - $\text{H}_2\text{O}$  inclusions (Bodnar, 2003), Table 1. Homogenization temperatures ranged from around  $31^\circ\text{C}$  for the  $\text{CO}_2$ -rich inclusions in GAP01:97, and the single-phased GAP01:219, which infers temperatures below  $50^\circ\text{C}$  (Roedder, 1984) to  $83.6^\circ\text{C}$  in GAP03:47,  $85.7$ – $140.1^\circ\text{C}$  in the  $\text{CaCl}_2$ - $\text{H}_2\text{O}$  inclusions of GAP01:97 m, up to the highest temperatures, which are from GAP01:74:  $198.7^\circ\text{C}$  and GAP04:305 m at  $163.1$ – $279.1^\circ\text{C}$ . The latter two samples also have significantly higher (and positive)  $\delta^{18}\text{O}_{\text{H}_2\text{O}}$  (SMOW) compared to the lower temperature inclusions.

#### 4.4. Biomarkers

Calcite from GAP01:30, GAP01:219, and GAP04:550 did not contain organic compounds in detectable amounts. The surface extract of calcite from GAP03:287, however, showed straight-chained and methyl branched fatty acids with 14–18 carbon atoms. Concentrations varied between 0.5 and  $139.3 \mu\text{g/g}$  calcite (Table 2). After calcite dissolution, a broader range of fatty acids with 12–18 carbon atoms was detected (Figure 7; Table 2). Additionally, the abundances significantly increased compared to the surface extract. At least 88% of each recovered fatty acid was trapped inside the calcite (100% for 12:0, 13:0, *iso*-14:0, 8-me-15:0, 10-me-15:0, and 15:1; Table 2). Little 16:0 ( $\leq 0.1 \mu\text{g}$ ) and 18:0 ( $\leq 0.3 \mu\text{g}$ ) appeared in the TMCS blank. The concentrations of these two compounds in the sample were corrected accordingly.

#### 4.5. U-Pb Geochronology

Two calcite samples yielded robust ages when targeted for high spatial resolution U-Pb geochronology using Laser Ablation Inductively Coupled Mass Spectrometry (LA-ICP-MS) in the same crystals that were targeted for SIMS microanalysis of C and O isotopes. Sample GAP01:219 yielded an age of  $75.2 \pm 7.4$  Ma (Figure 8a). This calcite shows no discernible growth zonation (Figure 4f), and the age is interpreted to represent a single calcite



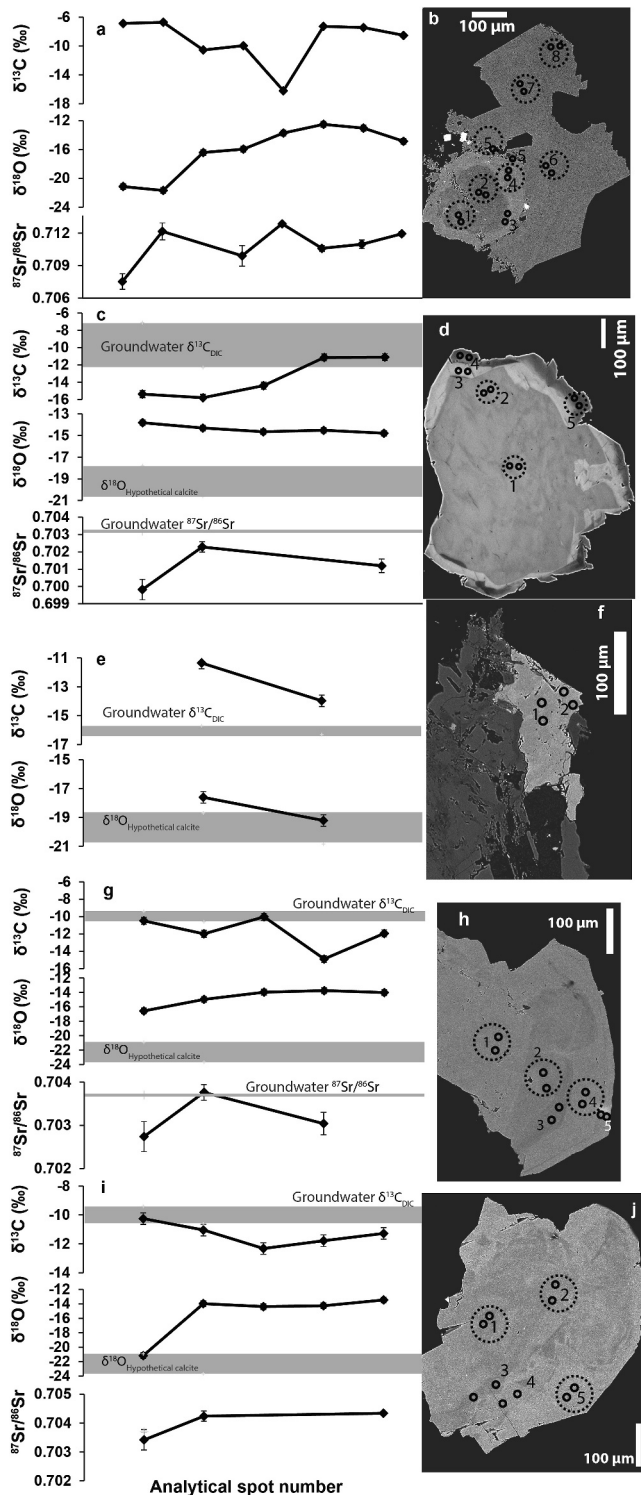


**Figure 4.** Micro-analytical transects for  $\delta^{13}\text{C}$ ,  $\delta^{18}\text{O}$ ,  $^{87}\text{Sr}/^{86}\text{Sr}$  within polished calcite crystals (spot locations marked on BSE-SEM images). Note the larger spot size for  $^{87}\text{Sr}/^{86}\text{Sr}$  spots (stippled circles, 80  $\mu\text{m}$ ) compared to  $\delta^{13}\text{C}$ ,  $\delta^{18}\text{O}$  (lined circles, 10  $\mu\text{m}$ ). Samples: (a) GAP01:30, (c) GAP04:550, (e) GAP01:219, (h) GAP04:636, (i) GAP04:681. Values of groundwater  $\delta^{13}\text{C}_{\text{DIC}}$  and hypothetical calcite  $\delta^{18}\text{O}$  using the current groundwater data and temperature (Harper et al., 2016) are also shown.

precipitation event. Sample GAP04:550 yielded an age of  $64.5 \pm 2.7$  Ma, and is derived from the inner, and most voluminous growth zone of the calcite crystals (the area covered by spots #1–3, Figure 4d), which means that there is a younger growth zone that is not dated.

## 5. Discussion

### 5.1. Sequence of Hydrothermal to Low-Temperature Events

The vein fillings and fracture coatings analyzed have formed at several events. The earliest groups are hydrothermal veins with calcite, pyrite, and quartz. This group has fluid inclusions with homogenization temperatures  $>150^\circ\text{C}$ , and high  $\delta^{18}\text{O}_{\text{H}_2\text{O}}$  (SMOW), which suggests metamorphic influence. The salinity are mostly low but range up to 11.6% in one occasion. The second group is distinguished by lower homogenization temperatures of  $83\text{--}140^\circ\text{C}$ , and higher salinity (23%–26%), which suggests a hydrothermal brine. The large  $\text{CO}_2$ -component of the fluid inclusions in dolomite of GAP01:97 m might suggest a magmatic source, but the low-temperature and relatively low  $\delta^{18}\text{O}_{\text{H}_2\text{O}}$  (SMOW) suggest there has been oxygen exchange with the host rock.  $\delta^{34}\text{S}_{\text{pyrite}}$  values of 0‰–4‰ for these older group veins are typical for hydrothermal pyrite (Field & Fifarek, 1985). The lack of radioisotopic dating inhibits any detailed interpretation of potential age and its relation to regional events. When compared to analog vein fillings from other Precambrian cratons, most of those with similar isotope signatures are Precambrian in age (Drake et al., 2009; Sandström et al., 2009), which is also plausible for the samples in this study. In addition, the (U-Th)/He zircon dates (220–580 Ma) determined for Western Greenland rocks imply several kilometers of burial of the basement by Paleozoic sediments (Danišik & Kirkland, 2023), which might have potentially increased the temperatures enough for hydrothermal fluid circulation and thermochemical sulfate reduction (TSR), and thus represent minimum ages for these fracture fills. As this older generation is hydrothermal, and the scope of this manuscript is on low-temperature circulation and paleomicrobial activity, the rest of the discussion will focus on the younger low-temperature generation of calcite/barite/pyrite/gypsum/clay minerals.

### 5.2. Relation of the Low-Temperature Fluid Circulation to Regional Tectonic Events

The dated samples with ages between 75 and 65 Ma represent a regional period of fracture opening and calcite precipitation that broadly coincides with the emplacement of the proto-Icelandic plume (Hestnes et al., 2023). Different models have shown that this plume could have caused uplift starting at c. 70 Ma (Barnett-Moore et al., 2018). Furthermore, regional rifting events may have begun at c. 81 Ma (Faleide et al., 2008), such as the opening of the Atlantic between Greenland and Norway, where structural and stratigraphic analyses suggest an early rift phase at c. 81 to 65 Ma that is characterized by large-scale normal faulting (Ren et al., 2003). Seafloor spreading between Greenland and Labrador commenced later, at c. 63–61 Ma (Chalmers & Pulvertaft, 2001; Lundin & Doré, 2005). This event featured a burst in volcanic activity, with large amounts of tholeiitic picrite and basalt eruptions onto the continental margins of West Greenland and Labrador (Melchior Larsen et al., 1999). The dated fracture minerals are thus overlapping in age with these large-scale events of regional rifting related to the opening of the Labrador Sea and early opening of the Atlantic Ocean.

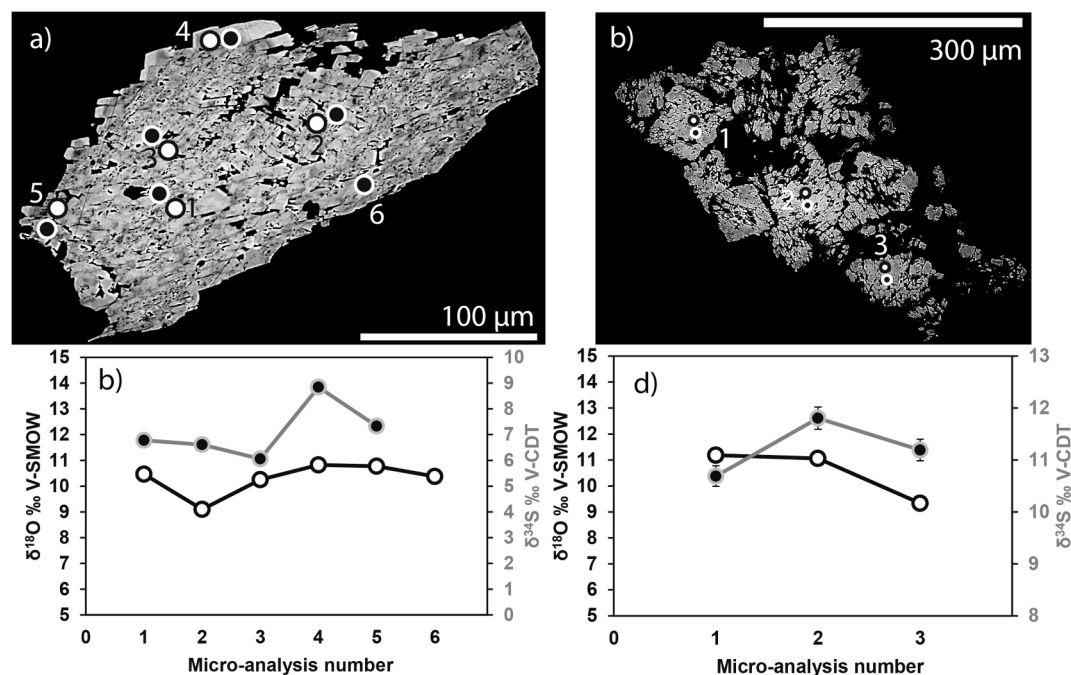


**Figure 5.** Secondary Ion Mass Spectrometry  $\delta^{34}\text{S}$  and  $\delta^{18}\text{O}$  transects for representative barite crystals with spot location in a and isotope values in (c) for sample GAP04:681, and (b, d) for GAP01:30. Black circles with white interiors are  $\delta^{18}\text{O}$  spots (values on left y-axis) and gray circles with black interiors are  $\delta^{34}\text{S}$  spots (values on right y-axis).

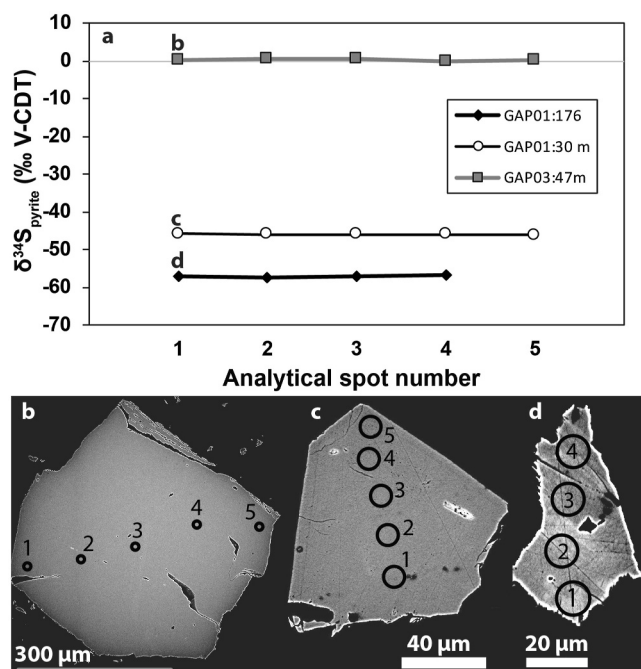


**Figure 6.**  $\delta^{34}\text{S}$  transects for representative pyrite crystals, for (b) hydrothermal pyrite, sample GAP03:47m, and (c, d) more fine-grained and very  $^{34}\text{S}$ -depleted pyrite (c, sample GAP01:30 and d GAP01:176).

### 5.3. Biosignatures for Microbial Sulfate Reduction at Depth

The generally large fractionation in the S isotope system ( $\delta^{34}\text{S}$ ) during MSR has made this system an extensively used tool for understanding both modern and ancient biogeochemical cycles (Bryant et al., 2019; Canfield & Farquhar, 2009; Johnston et al., 2006). This fractionation occurs due to discrimination of  $^{34}\text{S}$  compared to  $^{32}\text{S}$  by the microorganisms (Canfield, 2001), and is generally larger than the fractionation during abiotic thermochemical processes (Machel et al., 1995). Laboratory culture studies as well as environmental studies have reported depletion in  $^{32}\text{S}$  in sulfide relative to the source sulfate ( $^{34}\epsilon = \delta^{34}\text{S}_{\text{sulfate}} - \delta^{34}\text{S}_{\text{sulfide}}$ ) during MSR up to 75‰ (Canfield et al., 2010; Drake, Tullborg, et al., 2015; Sim et al., 2011; Wortmann et al., 2001). The MSR process enhances the saturation indices of iron sulfide minerals, which typically precipitate initially as mono-sulfides, evolving to metastable and usually poorly crystalline intermediates such as greigite and mackinawite, and ultimately to pyrite (Barrie et al., 2009; Thiel et al., 2019). Pyrite formed as an end result of MSR inherits the biological S isotope signature of the precursor hydrogen sulfide, as there is negligible fractionation during transformation from  $\text{FeS}$  to  $\text{FeS}_2$  (Böttcher et al., 1998), and thus,  $\delta^{34}\text{S}_{\text{pyrite}}$  commonly serves as an isotopic biomarker for MSR. The very low minimum  $\delta^{34}\text{S}_{\text{pyrite}}$  values (as low as  $-59\text{‰}$ ; Figure 6a) from the GAP samples are consequently proposed to result from large S isotope fractionation during MSR. The initial paleowater  $\delta^{34}\text{S}_{\text{sulfate}}$  is unknown, but the  $^{34}\epsilon$  can be estimated using the  $\delta^{34}\text{S}_{\text{barite}}$  and  $\delta^{34}\text{S}_{\text{gypsum}}$  in the fracture system. In particular, sample GAP01:30 is of interest, as there are coeval barite and pyrite on the same fracture surface (Figure 1i). The mean  $\delta^{34}\text{S}_{\text{barite}}$  values,

**Table 1**  
Fluid Inclusion Results, Carbonates

Sample	$T_c$ (°C)	$T_m$ (°C)	$T_h$ (°C)	Salinity	Paleofluid $\delta^{13}C_{CO_2}$ (PDB)	Paleofluid $\delta^{18}O_{H_2O}$ (SMOW)	FI type
GAP01:74	-21.3	-0.1	198.7	0.18	-5.46	3.31	NaCl-H <sub>2</sub> O
GAP01:97	-53.8	-33.1	140.1	23.6	-8.51	-4.50	CaCl <sub>2</sub> -H <sub>2</sub> O
GAP01:97	-50.1	-27.2	85.7	26.3	-11.46	-9.77	CaCl <sub>2</sub> -H <sub>2</sub> O
GAP01:97	-52.1	-26.8	96.1	26.2	-10.77	-8.58	CaCl <sub>2</sub> -H <sub>2</sub> O
GAP01:97	-56.6	-	31.4	-	-	-	CO <sub>2</sub>
GAP01:97	-56.6	-	31.4	-	-	-	CO <sub>2</sub>
GAP01:97	-56.3	-	31.3	-	-	-	CO <sub>2</sub>
GAP01:97	-56.4	-	31.2	-	-	-	CO <sub>2</sub>
GAP01:219	-	-	<50	2.2-4.7	-	-	NaCl-H <sub>2</sub> O
GAP03:47	-	-	83.6	-	-12.46	-5.87	CaCl <sub>2</sub> -H <sub>2</sub> O
GAP03:305 m	-27.8	-7.9	279.1	11.6	-7.77	9.75	NaCl-H <sub>2</sub> O
GAP03:305 m	-22.7	-1.1	163.1	1.90	-10.42	4.22	NaCl-H <sub>2</sub> O

$T_c$ =First ice melting temperature,  $T_m$ =Final ice melting temperature,  $T_h$ =Homogenization temperature, FI=Fluid inclusion. Isotopic signatures of paleo-fluids are calculated using the fluid inclusion  $T_h$  temperatures and fractionation factor—temperature equations for CO<sub>2</sub>-CaCO<sub>3</sub> (Bottinga, 1968) and CaCO<sub>3</sub>-H<sub>2</sub>O (O'Neil et al., 1969), respectively.

+13.0 ± 1.9‰, and  $\delta^{34}S_{pyrite}$  values, -55.1 ± 2.0‰ of this sample will give a mean  $^{34}\epsilon = \delta^{34}S_{sulfate} - \delta^{34}S_{sulfide}$  of 68.1‰ (up to a maximum of 75.3‰, when taking the full range of the SIMS values). In comparison, the mean  $\delta^{34}S_{barite}$  value is overlapping or slightly lower than contemporary Late-Cretaceous-Early Paleocene seawater sulfate (17–20‰, based on sedimentary  $\delta^{34}S_{barite}$  values, Present et al., 2020). A  $^{34}\epsilon$  value of 68‰ to explain the

**Table 2**  
Concentrations of Fatty Acids in Calcite Coating GAP03:287

	Surface extract c (µg/g)	Dissolved calcite c (µg/g)	Calcite-trapped portion (%)
12:0	-	15.7	100
13:0	-	12.5	100
<i>i</i> -14:0	-	4.3	100
14:1	0.5	10.7	96
14:0	5.2	224.3	98
8Me-14:0	-	11.3	100
4Me-14:0	0.5	37.6	99
10Me-14:0	-	19.4	100
<i>i</i> -15:0	1.1	38.1	97
<i>ai</i> -15:0	2.6	107.6	98
15:1	-	39.8	100
15:0	4.3	317.0	99
<i>i</i> -16:0	2.0	55.6	97
16:1	17.3	508.2	97
16:0	139.3	2,597.7	95
4Me-16:0	2.4	68.0	97
10Me-16:0	1.0	42.3	98
17:0	3.5	75.6	96
18:2	7.6	53.3	88
18:1	62.4	918.4	94
18:0	78.9	1,184.6	94

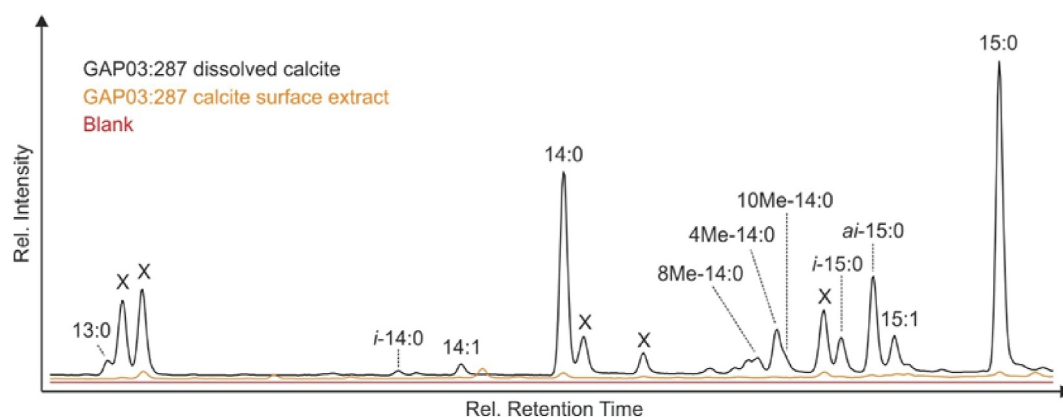


**Figure 7.** Specific fatty acids in calcite from GAP03:287 (section of the total ion chromatogram). *i*-14:0, 10Me-14:0, *i*-15:0, and *ai*-15:0 are indicative of sulfate reducers. The GAP03:287 calcite surface extract (orange line) and the blank (red line) are shown for comparison.

$\delta^{34}\text{S}_{\text{pyrite}}$  values in GAP01:30, is in line with  $^{34}\epsilon$  observed for MSR-induced pyrite precipitation in 415 m deep groundwater at Äspö, SE Sweden (Drake, Tullborg, et al., 2015), and for coexisting dissolved sulfide and sulfate from hypersulfidic interstitial waters in a sediment core from the continental margin of the Great Australian Bight that shows an isotope difference of up to 72‰ caused by in situ MSR (Wortmann et al., 2001). Formation of the sulfide by TSR can be ruled out as it produces  $^{34}\epsilon$  of up to 22‰, but usually much less (Kiyosu & Krouse, 1990). For the other samples with extremely low  $\delta^{34}\text{S}_{\text{pyrite}}$  values, there are no corresponding  $\delta^{34}\text{S}_{\text{sulfate}}$  measured, inhibiting direct comparisons of sulfate and sulfide  $\delta^{34}\text{S}$  on the sample scale. The deeper barite sample GAP04:681 had lower  $\delta^{34}\text{S}$  values,  $6.9 \pm 0.8\text{‰}$ , than GAP01:30, and is within the range of gypsum measured in the same borehole section (values between +2.6 and +10.7‰, Harper et al., 2016; Henkemans, 2016). Applying these lower values would give a minimum  $\epsilon^{34}\text{S}$  of 49.3 and 57.3‰ for the lightest  $\delta^{34}\text{S}_{\text{pyr}}$  of GAP01:176, 57.6‰ for GAP01:219, and 42.0‰ for GAP03:287, respectively, which all agree with MSR. The small  $\delta^{34}\text{S}_{\text{pyrite}}$  differences within the individual pyrite crystals suggest that MSR occurred in an open system with regard to sulfate and/or at high sulfate concentrations, which promotes high S fractionation during MSR (Leavitt et al., 2013). The sulfate concentrations in the groundwater of the boreholes are indeed relatively high up to almost 2,000 mg/L at large depth in GAP04 (Harper et al., 2016). Closed system Rayleigh distillations would theoretically also affect barite by increasing the  $\delta^{34}\text{S}_{\text{barite}}$  values as the sulfate pool diminishes (Magnall et al., 2016). The relatively homogeneous  $\delta^{34}\text{S}$  (and  $\delta^{18}\text{O}$ ) values within individual barite grains (Figure 5) are therefore another supporting line of evidence for MSR in open

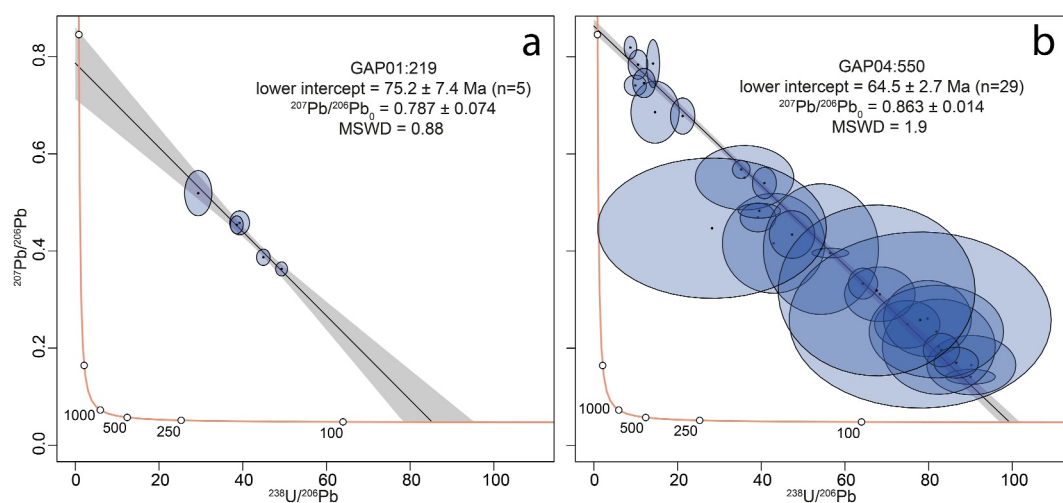


**Figure 8.** U-Pb dating of calcite sample GAP01:219 (a), and GAP04:550 (b). Ages reflect lower intercept ages and uncertainties are quoted at 2 sigma and comprise systematic uncertainties. Data details are reported in Table S9 in Supporting Information S1.



and/or sulfate rich conditions. Taken together, MSR is supported by the low  $\delta^{34}\text{S}_{\text{pyrite}}$  and high apparent isotope enrichment between precipitated sulfate and sulfide minerals, and MSR appears to have occurred in an open system and/or at high concentrations of dissolved sulfate.

Additionally, calcite from GAP03:287 incorporated several fatty acids, including *i*-14:0, 10Me-14:0, *i*-15:0, *ai*-15:0, 4Me-16:0, and 10Me-16:0 (Figure 7; Table 2), which are typically found in sulfate reducers (Dowling et al., 1986; Kaksonen et al., 2006; So & Young, 1999; Ueki & Suto, 1979). The presence of 10Me-14:0, 4Me-16:0, and 10Me-16:0 may even indicate a hydrocarbon-based metabolism (So & Young, 1999). Moreover, organotrophic sulfate reduction is indicated by  $\delta^{13}\text{C}$ -depleted calcite coatings in the samples with MSR-related  $\delta^{34}\text{S}_{\text{pyr}}$ -values (GAP01:30, down to  $-16.2\%$ ; GAP01:219:  $-14.0\%$ , GAP03:287:  $-13.5\%$ , GAP01:176, no calcite). Thus, there are several lines of evidence in support of ancient MSR in the deep fracture system.

#### 5.4. Timing of Microbial Activity

The U-Pb age of GAP01:219 calcite occurring together with MSR-related pyrite suggests that MSR occurred in the fracture system in the late Cretaceous ( $75.2 \pm 7.4$  Ma). GAP04:550 yielded a slightly younger age of  $64.5 \pm 2.7$  Ma, which shows that fluid flow and mixing that induced mineral precipitation occurred at the Cretaceous-Paleogene boundary in the bedrock fracture systems of Western Greenland. Extension-related opening of normal faults enabled the descent of microbial communities in fresh water that mixed with deeper seated brines. This scenario shares similarities with observations from the Fennoscandian shield (Drake et al., 2023; Sahlstedt et al., 2013; Sandström & Tullborg, 2009) and sedimentary basins in North America (Budai et al., 2002; Martini et al., 1998; McIntosh et al., 2023).

Although the GAP fracture coatings apparently range from numerous generations of hydrothermal to low-temperature precipitates with host rocks dating back to the Archean, it is notable that only the young fracture-hosted low-temperature calcite appears together with co-genetic MSR-related pyrite. Older coatings lack biosignatures for microbial activity. Thermochronology investigations provide a powerful tool to assess the habitability of the rock volume over time, helping to understand the local subterranean paleomicrobiology (Drake & Reiners, 2021). Periods of subsidence due to sedimentary rock coverage may have depressed the bedrock volume to depths that infer temperatures above the limit of life ( $122^\circ\text{C}$ , Takai et al., 2008) for long times during the geological history of the area. Thermochronology studies from Western Greenland predict that ambient conditions prevailed during formation of the fracture coating calcites, following earlier periods of subsidence and inhabitable temperatures (Danišik & Kirkland, 2023; Jess et al., 2018). Thermal processes associated with extensional tectonism starting in the Late Triassic and passive margin formation in the Early Cretaceous have been indicated, but there is no evidence of thermal activity during Cenozoic times in the area (Danišik & Kirkland, 2023). This suggests that the temperature was suitable for microbial colonization at the time of formation of the dated calcite crystals (i.e., Cretaceous-Paleogene), but it was periodically too hot before. However, some habitable windows in earlier geological periods seem plausible. Mean zircon (U-Th)/He dates from ca. 725 Ma to ca. 1.05 Ga record exhumation of the basement to upper crustal levels during Meso-/Neoproterozoic times following the Nagssugtoqidian orogeny at 1.7 Ga (Danišik & Kirkland, 2023), but no biosignatures for deep subsurface microbial activity from these times have been found.

#### 5.5. Potential Modern Glacial Water-Associated Precipitates

The isotope composition of the fracture coating minerals, in particular O and Sr of calcite, can be compared with the chemical composition of the groundwater to assess whether the minerals might be precipitated from modern groundwater (Drake, Ivarsson, et al., 2018; Sahlstedt et al., 2016; Sandström & Tullborg, 2009; Tullborg et al., 1999; Wallin & Peterman, 1999). Although  $\delta^{13}\text{C}$ -DIC values of the groundwater (Harper et al., 2016) roughly match with the  $\delta^{13}\text{C}_{\text{calcite}}$  range (Figure 3a), and Quaternary glacial water has likely influenced a few fracture flow paths below the permafrost in GAP04 (Drake, Suksi, et al., 2017), no agreement can be observed for  $\delta^{18}\text{O}$  (Figure 3b applying temperature-based fractionation factors from Kim & O'Neil, 1997 and simple flushing water contamination correction for GAP04 upper and middle sections). Due to the potential flushing water contamination, these comparisons (upper and middle section) should be taken with caution. The groundwater sampling and potential causes of contamination are the subject of another ongoing study. The SIMS analyses enabled comparison between the outermost growth zones and the groundwater (Figure 4) and showed correspondence in some rare cases.

Considering the  $^{87}\text{Sr}/^{86}\text{Sr}$  data, some calcite (Figure 3d) shows an overlap with the groundwater  $^{87}\text{Sr}/^{86}\text{Sr}$  values, which may indicate precipitation from the present-day waters. However, this is contradicted by the different  $\delta^{18}\text{O}$  values between calcite and groundwater. Calcite sample GAP04:550 (Figure 4c) for example, which was recovered from a hydraulically active part underneath the permafrost, shows slightly less radiogenic values than the groundwater. This suggests that the calcite is not modern but precipitated from an ancient groundwater that has not evolved to the radiogenic levels encountered in the present groundwater. Generally, Quaternary glacial waters have made very little imprint in the calcite record of the fractures below and in the vicinity of the continental ice sheet and permafrost. Instead, the low temperature precipitates are indicated to be Cretaceous-Paleogene in age, as suggested by the two dated calcite samples.

## 6. Conclusions

Several generations of secondary mineral precipitates can be attested in deep fracture networks in the Archean rocks of the Kangerlussuaq area in Western Greenland. At least one of these generations is Cretaceous-Paleogene in age and is proposed to be temporally tied to extensional tectonics related to the opening of the North Atlantic and Labrador Sea. Potential glacial water precipitates have not been documented in the present study but cannot be ruled out. The Cretaceous-Paleogene calcite-pyrite-associations contain MSR signatures (isotopic fingerprints and molecular biomarkers). It is therefore indicated that the extensional tectonics related to the opening of the North Atlantic and Labrador Sea enabled the colonization of the fracture system by microorganisms via fluid infiltration.

## Data Availability Statement

All data are available in the supplementary information and deposited in the Swedish National Data Service repository.

## Acknowledgments

We are grateful to the Swedish Nuclear Fuel and Waste Management Co. (SKB), Posiva Oy, NWMO for access to samples and fluid data, and to the Swedish Research Council (VR, contract 2021–04365), FORMAS (contract 2020-01577), J. Gust. Richert foundation (contract 2023-00850), NSF FRES SMRFS Grant (EAR 2120733), and the Crafoord foundation (contract 20210524) for financial support. We also acknowledge VR for financial support to the NordSIMS-Vegacenter national research infrastructure (Grant 2021-00276). We thank Kerstin Lindén and Heejin Jeon for assistance with SIMS sample preparation and analysis, Lillemor Claesson Liljedahl and Anne Kontula for discussions of water chemistry and data, Melanie Kielman-Schmitt for assistance during LA-MC-ICP-MS-analysis, and Paula Lake for assistance during organic-geochemical preparation. We thank Scott Perl and an anonymous reviewer for constructive comments. This is NordSIMS publication 765 and Vegacenter publication 078.

## References

- Al-Aasm, I. S., Taylor, B. E., & South, B. (1990). Stable isotope analysis of multiple carbonate samples using selective acid extraction. *Chemical Geology: Isotope Geoscience section*, 80(2), 119–125. [https://doi.org/10.1016/0168-9622\(90\)90020-d](https://doi.org/10.1016/0168-9622(90)90020-d)
- Andrews, M. G., Jacobson, A. D., Lehn, G. O., Horton, T. W., & Craw, D. (2016). Radiogenic and stable Sr isotope ratios ( $^{87}\text{Sr}/^{86}\text{Sr}$ ,  $\delta^{88}\text{Sr}$ ) as tracers of riverine cation sources and biogeochemical cycling in the Milford Sound region of Fiordland, New Zealand. *Geochimica et Cosmochimica Acta*, 173, 284–303. <https://doi.org/10.1016/j.gca.2015.10.005>
- Barnett-Moore, N., Müller, D. R., Williams, S., Skogseid, J., & Seton, M. (2018). A reconstruction of the North Atlantic since the earliest Jurassic. *Basin Research*, 30(S1), 160–185. <https://doi.org/10.1111/bre.12214>
- Barrie, C. D., Boyce, A. J., Boyle, A. P., Williams, P. J., Blake, K., Ogawara, T., et al. (2009). Growth controls in colloform pyrite. *American Mineralogist*, 94(4), 415–429. <https://doi.org/10.2138/am.2009.3053>
- Bengtson, S., Ivarsson, M., Astolfo, A., Belivanova, V., Broman, C., Marone, F., & Stampanoni, M. (2014). Deep-biosphere consortium of fungi and prokaryotes in Eocene subseafloor basalts. *Geobiology*, 12(6), 489–496. <https://doi.org/10.1111/gbi.12100>
- Blyth, A., Frapé, S., Blomqvist, R., & Nissinen, P. (2000). Assessing the past thermal and chemical history of fluids in crystalline rock by combining fluid inclusion and isotopic investigations of fracture calcite. *Applied Geochemistry*, 15(10), 1417–1437. [https://doi.org/10.1016/S0883-2927\(00\)00007-x](https://doi.org/10.1016/S0883-2927(00)00007-x)
- Blyth, A., Frapé, S., Ruskeeniemi, T., & Blomqvist, R. (2004). Origins, closed system formation and preservation of calcites in glaciated crystalline bedrock; evidence from the Palmottu natural analogue site, Finland. *Applied Geochemistry*, 19(5), 675–686. <https://doi.org/10.1016/j.apgeochem.2003.07.004>
- Blyth, A. R., Frapé, S. K., Ruskeeniemi, T., & Blomqvist, R. (2002). Long-term hydrogeological stability of crystalline bedrock in glaciated terrains; evidence from the Palmottu natural analogue research site, Finland. In *Geological Society of America, 2002 annual meeting* (pp. 498–499). Geological Society of America (GSA).
- Bodnar, R. J. (2003). Introduction to aqueous-electrolyte fluid inclusions. In I. Samson, A. Anderson, & D. Marshall (Eds.), *Fluid inclusions: Analysis and interpretation* (pp. 81–99). Mineralogical Association of Canada.
- Bomberg, M., Claesson, L. L., Lamminmäki, T., & Kontula, A. (2019). Highly diverse Aquatic microbial communities separated by permafrost in Greenland show distinct features according to environmental Niches. *Frontiers in Microbiology*, 10, 1583. <https://doi.org/10.3389/fmicb.2019.01583>
- Bonow, J. M., Lidmar-Bergström, K., & Japsen, P. (2006). Palaeosurfaces in central West Greenland as reference for identification of tectonic movements and estimation of erosion. *Global and Planetary Change*, 50(3–4), 161–183. <https://doi.org/10.1016/j.gloplacha.2005.12.011>
- Böttcher, M. E., Smock, A. M., & Cypionka, H. (1998). Sulfur isotope fractionation during experimental precipitation of iron(II) and manganese (II) sulfide at room temperature. *Chemical Geology*, 146(3–4), 127–134. [https://doi.org/10.1016/S0009-2541\(98\)00004-7](https://doi.org/10.1016/S0009-2541(98)00004-7)
- Bottinga, Y. (1968). Calculation of fractionation factors for carbon and oxygen isotopic exchange in the system calcite–carbon dioxide–water. *Journal of Physical Chemistry*, 72(3), 800–808. <https://doi.org/10.1021/j100849a008>
- Brown, J., Ferrians, O. J., Heginbottom, J. A., & Melnikov, E. S. (1998). Circum-arctic map of permafrost and ground ice conditions. In *National Snow and ice data center/World data center for glaciology*. Digital media.
- Bryant, R. N., Jones, C., Raven, M. R., Gomes, M. L., Berelson, W. M., Bradley, A. S., & Fike, D. A. (2019). Sulfur isotope analysis of microcrystalline iron sulfides using secondary ion mass spectrometry imaging: Extracting local paleo-environmental information from modern and ancient sediments. *Rapid Communications in Mass Spectrometry*, 33(5), 491–502. <https://doi.org/10.1002/rcm.8375>

- Budai, J. M., Martini, A. M., Walter, L. M., & Ku, T. C. W. (2002). Fracture-fill calcite as a record of microbial methanogenesis and fluid migration; a case study from the Devonian Antrim Shale, Michigan Basin. *Geofluids*, 2(3), 163–183. <https://doi.org/10.1046/j.1468-8123.2002.00036.x>
- Cabral, R. A., Jackson, M. G., Rose-Koga, E. F., Koga, K. T., Whitehouse, M. J., Antonelli, M. A., et al. (2013). Anomalous sulphur isotopes in plume lavas reveal deep mantle storage of Archaean crust. *Nature*, 496(7446), 490–493. <https://doi.org/10.1038/nature12020>
- Cadman, A. C., Tarney, J., Bridgwater, D., Mengel, F., Whitehouse, M. J., & Windley, B. F. (2001). The petrogenesis of the Kangamiut dyke swarm, W. Greenland. *Precambrian Research*, 105(2–4), 183–203. [https://doi.org/10.1016/s0301-9268\(00\)00111-x](https://doi.org/10.1016/s0301-9268(00)00111-x)
- Canfield, D. E. (2001). Isotope fractionation by natural populations of sulfate-reducing bacteria. *Geochimica et Cosmochimica Acta*, 65(7), 1117–1124. [https://doi.org/10.1016/s0016-7037\(00\)00584-6](https://doi.org/10.1016/s0016-7037(00)00584-6)
- Canfield, D. E., & Farquhar, J. (2009). Animal evolution, bioturbation, and the sulfate concentration of the oceans. *Proceedings of the National Academy of Sciences*, 106(20), 8123–8127. <https://doi.org/10.1073/pnas.0902037106>
- Canfield, D. E., Farquhar, J., & Zerkle, A. L. (2010). High isotope fractionations during sulfate reduction in a low-sulfate euxinic ocean analog. *Geology*, 38(5), 415–418. <https://doi.org/10.1130/g30723.1>
- Carlsson, D.-T., Ivarsson, M., & Neubeck, A. (2019). Fossilized endolithic microorganisms in pillow lavas from the Troodos ophiolite, Cyprus. *Geosciences*, 9(11), 456. <https://doi.org/10.3390/geosciences9110456>
- Chalmers, J. A., & Pulvertaft, T. C. R. (2001). Development of the continental margins of the Labrador Sea: A review. In R. C. L. Wilson, R. B. Whitmarsh, B. Taylor, & N. Froitzheim (Eds.), *Nonvolcanic rifting of continental margins: A comparison of evidence from Land and sea* (pp. 77–105). Geological Society of London, Special Publications.
- Claesson Liljedahl, L., Kontula, A., Harper, J., Näslund, J.-O., Selroos, J.-O., Pitkänen, P., et al. (2016). The Greenland Analogue project: Final report, SKB report TR-14-13.
- Clauer, N., Frapé, S. K., & Fritz, B. (1989). Calcite veins of the Stripa granite (Sweden) as records of the origin of the groundwaters and their interactions with the granitic body. *Geochimica et Cosmochimica Acta*, 53(8), 1777–1781. [https://doi.org/10.1016/0016-7037\(89\)90298-6](https://doi.org/10.1016/0016-7037(89)90298-6)
- Connolly, J. A. D. (1997). Devolatilization-generated fluid pressure and deformation-propagated fluid flow during prograde regional metamorphism. *Journal of Geophysical Research, B, Solid Earth and Planets*, 102(B8), 18149–18173. <https://doi.org/10.1029/97jb00731>
- Coplen, T. B. (1995). Reporting of stable hydrogen, carbon, and oxygen isotopic abundances. *Geothermics*, 24(5–6), 707–712. [https://doi.org/10.1016/0375-6505\(95\)00024-0](https://doi.org/10.1016/0375-6505(95)00024-0)
- Danišák, M., & Kirkland, C. L. (2023). Thermochronometry constraints on south West Greenland passive continental margin development. *Communications Earth & Environment*, 4(1), 124. <https://doi.org/10.1038/s43247-023-00786-6>
- Ding, T., Valkiers, S., Kipphardt, H., De Bievre, P., Taylor, P. D. P., Gonfiantini, R., & Krouse, R. (2001). Calibrated sulfur isotope abundance ratios of three IAEA sulfur isotope reference materials and V-CDT with a reassessment of the atomic weight of sulfur. *Geochimica et Cosmochimica Acta*, 65(15), 2433–2437. [https://doi.org/10.1016/s0016-7037\(01\)00611-1](https://doi.org/10.1016/s0016-7037(01)00611-1)
- Di Salvo, S., Braschi, E., Casalini, M., Marchionni, S., Adani, T., Ulivi, M., et al. (2018). High-precision in situ <sup>87/86</sup>Sr analyses through Microsampling on solid samples: Applications to Earth and Life Sciences. *Journal of Analytical Methods in Chemistry*, 2018, 1292954.
- Dowling, N. J. E., Widdel, F., & White, D. C. (1986). Phospholipid ester-linked fatty acid biomarkers of acetate-oxidizing sulphate-reducers and other sulphide-forming bacteria. *Journal of General Microbiology*, 132(7), 1815–1825. <https://doi.org/10.1099/00221287-132-7-1815>
- Drake, H., Åström, M. E., Heim, C., Broman, C., Åström, J., Whitehouse, M. J., et al. (2015). Extreme <sup>13</sup>C-depletion of carbonates formed during oxidation of biogenic methane in fractured granite. *Nature Communications*, 6(1), 7020. <https://doi.org/10.1038/ncomms8020>
- Drake, H., Heim, C., Roberts, N. M. W., Zack, T., Tillberg, M., Broman, C., et al. (2017). Isotopic evidence for microbial production and consumption of methane in the upper continental crust throughout the Phanerozoic eon. *Earth and Planetary Science Letters*, 470, 108–118. <https://doi.org/10.1016/j.epsl.2017.04.034>
- Drake, H., Ivarsson, M., Heim, C., Snoeyenbos-West, O., Bengtson, S., Belivanova, V., & Whitehouse, M. (2021). Fossilized anaerobic and possibly methanogenesis-fueled fungi identified deep within the Siljan impact structure, Sweden. *Communications Earth & Environment*, 2(1), 34. <https://doi.org/10.1038/s43247-021-00107-9>
- Drake, H., Ivarsson, M., Tillberg, M., Whitehouse, M., & Kooijman, E. (2018). Ancient microbial activity in deep hydraulically conductive fracture zones within the Forsmark Target area for geological nuclear waste Disposal, Sweden. *Geosciences*, 8(6), 211. <https://doi.org/10.3390/geosciences8060211>
- Drake, H., Kooijman, E., & Kielman-Schmitt, M. (2020). Using <sup>87</sup>Sr/<sup>86</sup>Sr LA-MC-ICP-MS transects within modern and ancient calcite crystals to determine fluid flow events in deep granite fractures. *Geosciences*, 10(9), 345. <https://doi.org/10.3390/geosciences10090345>
- Drake, H., & Reiners, P. W. (2021). Thermochronologic perspectives on the deep-time evolution of the deep biosphere. *Proceedings of the National Academy of Sciences*, 118(45), e2109609118. <https://doi.org/10.1073/pnas.2109609118>
- Drake, H., Roberts, N. M. W., Heim, C., Whitehouse, M. J., Siljeström, S., Kooijman, E., et al. (2019). Timing and origin of natural gas accumulation in the Siljan impact structure, Sweden. *Nature Communications*, 10(1), 4736. <https://doi.org/10.1038/s41467-019-12728-y>
- Drake, H., Roberts, N. M. W., Reinhardt, M., Whitehouse, M., Ivarsson, M., Karlsson, A., et al. (2021). Biosignatures of ancient microbial life are present across the igneous crust of the Fennoscandian shield. *Communications Earth & Environment*, 2(1), 102. <https://doi.org/10.1038/s43247-021-00170-2>
- Drake, H., Suksi, J., Tullborg, E.-L., & Lahaye, Y. (2017). Quaternary redox transitions in deep crystalline rock fractures at the Western margin of the Greenland ice sheet. *Applied Geochemistry*, 76, 196–209. <https://doi.org/10.1016/j.apgeochem.2016.12.001>
- Drake, H., Tillberg, M., Reinhardt, M., Whitehouse, M. J., & Kooijman, E. (2023). In situ Rb/Sr geochronology and stable isotope geochemistry evidence for neoproterozoic and paleozoic fracture-hosted fluid flow and microbial activity in paleoproterozoic basement, SW Sweden. *Geochemistry, Geophysics, Geosystems*, 24(5), e2023GC010892. <https://doi.org/10.1029/2023gc010892>
- Drake, H., Tullborg, E.-L., & Page, L. (2009). Distinguished multiple events of fracture mineralisation related to far-field orogenic effects in Paleoproterozoic crystalline rocks, Simpevarp area, SE Sweden. *Lithos*, 110(1–4), 37–49. <https://doi.org/10.1016/j.lithos.2008.12.003>
- Drake, H., Tullborg, E.-L., Sandberg, B., Blomfeldt, T., Åström, M. E., & Åström, M. E. (2015). Extreme fractionation and micro-scale variation of sulphur isotopes during bacterial sulphate reduction in Deep groundwater systems. *Geochimica et Cosmochimica Acta*, 161, 1–18. <https://doi.org/10.1016/j.gca.2015.04.014>
- Drake, H., Whitehouse, M. J., Heim, C., Reiners, P. W., Tillberg, M., Hogmalm, K. J., et al. (2018). Unprecedented <sup>34</sup>S-enrichment of pyrite formed following microbial sulfate reduction in fractured crystalline rocks. *Geobiology*, 16(5), 556–574. <https://doi.org/10.1111/gbi.12297>
- Engström, J., & Klint, K. E. S. (2014). Continental collision structures and post-orogenic geological history of the Kangerlussuaq area in the southern part of the Nagssugtoqidian orogen, central west Greenland. *Geosciences*, 4, 316–334. <https://doi.org/10.3390/geosciences4040316>
- Escher, A., Escher, J. C., & Watterson, J. (1975). The reorientation of the Kangamiut dyke swarm, west Greenland. *Canadian Journal of Earth Sciences*, 12(2), 158–173. <https://doi.org/10.1139/e75-016>

- Escher, A., Sørensen, K., & Zeck, H. P. (1976). Nagssugtoqidian mobile belt in West Greenland. In A. Escher & W. S. Watt (Eds.), *Geology of Greenland* (pp. 77–95). Geological Survey of Greenland.
- Faleide, J. I., Tsikalas, F., Breivik, A. J., Mjelde, R., Ritzmann, O., Engen, Ø., et al. (2008). Structure and evolution of the continental margin off Norway and the Barents Sea. *International Union of Geological Sciences*, 31(1), 82–91. <https://doi.org/10.18814/epiugs/2008/v31i1/012>
- Field, C. W., & Fifarek, R. H. (1985). Light stable-isotopes systematics in the epithermal environment. *Reviews in Economic Geology*, 2, 99–128.
- French, H. M. (2007). *The periglacial environment* (3rd ed.). John Wiley & Sons.
- Garde, A. A., & Hollis, J. A. (2010). A buried Palaeoproterozoic spreading ridge in the northern Nagssugtoqidian orogen, West Greenland. In T. M. Kusky, M.-G. Zhai, & W. Xiao (Eds.) *The evolving continents: Understanding processes of continental growth; special publications* (Vol. 338, pp. 213–234). Geological Society of London. <https://doi.org/10.1144/sp338.11>
- Garde, A. A., & Marker, M. (2010). *Geological map of Greenland: Sandflugtdalen–Nuussuaq; map sheet, 1:500000*. Geological Survey of Denmark and Greenland.
- Gimeno, M. J., Tullborg, E.-L., Nilsson, A.-C., Auqué, L. F., & Nilsson, L. (2023). Hydrogeochemical characterisation of the groundwater in the crystalline basement of Forsmark, the selected area for the geological nuclear repositories in Sweden. *Journal of Hydrology*, 624, 129818. <https://doi.org/10.1016/j.jhydrol.2023.129818>
- Gómez, J. B., Gimeno, M. J., Auqué, L. F., & Acero, P. (2014). Characterisation and modelling of mixing processes in groundwaters of a potential geological repository for nuclear wastes in crystalline rocks of Sweden. *Science of the Total Environment*, 468–469, 791–803. <https://doi.org/10.1016/j.scitotenv.2013.09.007>
- Harper, J., Hubbard, A., Ruskeeniemi, T., Claesson, L. L., Kontula, A. M. H., Brown, J., et al. (2016). *The Greenland analogue project: Data and processes, SKB R-14-13*. Swedish Nuclear Fuel and Waste Management Company.
- Heim, C., Lausmaa, J., Sjövall, P., Toporski, J., Dieing, T., Simon, K., et al. (2012). Ancient microbial activity recorded in fracture fillings from granitic rocks (Åspö Hard Rock Laboratory, Sweden). *Geobiology*, 10(4), 280–297. <https://doi.org/10.1111/j.1472-4669.2012.00328.x>
- Heinonen, A., Andersen, T., Rämö, O. T., & Whitehouse, M. (2015). The source of Proterozoic anorthosite and rapakivi granite magmatism: Evidence from combined in situ Hf–O isotopes of zircon in the Ahvenisto complex, southeastern Finland. *Journal of the Geological Society*, 172(1), 103–112. <https://doi.org/10.1144/jgs2014-013>
- Henkemans, E. (2016). *Geochemical characterization of groundwaters, surface waters and water-rock interaction in an area of continuous permafrost adjacent to the Greenland ice sheet, Kangerlussuaq, southwest Greenland (PhD Thesis)*. University of Waterloo.
- Henkemans, E., Frapé, S. K., Ruskeeniemi, T., Anderson, N. J., & Hobbs, M. (2018). A landscape-isotopic approach to the geochemical characterization of lakes in the Kangerlussuaq region, west Greenland. *Arctic Antarctic and Alpine Research*, 50(1), S100018. <https://doi.org/10.1080/15230430.2017.1420863>
- Hestnes, Å., Drost, K., Sømme, T. O., Gasser, D., Scheiber, T., Linge, H., et al. (2023). Constraining the tectonic evolution of rifted continental margins by U–Pb calcite dating. *Scientific Reports*, 13(1), 7876. <https://doi.org/10.1038/s41598-023-34649-z>
- Hill, C. A., Polyak, V. J., Asmerom, Y., & P. Provencio, P. (2016). Constraints on a Late Cretaceous uplift, denudation, and incision of the Grand Canyon region, southwestern Colorado Plateau, USA, from U–Pb dating of lacustrine limestone. *Tectonics*, 35(4), 896–906. <https://doi.org/10.1002/2016tc004166>
- Holland, G., Lollar, B. S., Li, L., Lacrampe-Couloume, G., Slater, G. F., & Ballentine, C. J. (2013). Deep fracture fluids isolated in the crust since the Precambrian era. *Nature*, 497(7449), 357–360. <https://doi.org/10.1038/nature12127>
- Horstwood, M. S. A., Košler, J., Gehrels, G., Jackson, S. E., McLean, N. M., Paton, C., et al. (2016). Community-derived standards for LA-ICP-MS U–(Th)–Pb geochronology – Uncertainty propagation, age interpretation and data reporting. *Geostandards and Geoanalytical Research*, 40(3), 311–332. <https://doi.org/10.1111/j.1751-908x.2016.00379.x>
- Horwitz, P., Chiarizia, R., & Dietz, M. L. (1992). A novel strontium-selective extraction chromatographic resin. *Solvent Extraction and Ion Exchange*, 10(2), 313–336. <https://doi.org/10.1080/07366299208918107>
- Horwitz, P., Dietz, M. L., Rhoads, S., Felinto, C., Gale, N. H., & Houghton, J. (1994). A lead-selective extraction chromatographic resin and its application to the isolation of lead from geological samples. *Analytica Chimica Acta*, 292(3), 263–273. [https://doi.org/10.1016/0003-2670\(94\)00068-9](https://doi.org/10.1016/0003-2670(94)00068-9)
- Hubalek, V., Wu, X., Eiler, A., Buck, M., Heim, C., Dopson, M., et al. (2016). Connectivity to the surface determines diversity patterns in subsurface aquifers of the Fennoscandian shield. *The ISME Journal*, 10(10), 2447–2458. <https://doi.org/10.1038/ismej.2016.36>
- Ivarsson, M., Bengtson, S., Skogby, H., Belivanova, V., & Marone, F. (2013). Fungal colonies in open fractures of seafloor basalt. *Geo-Marine Letters*, 33(4), 233–234. <https://doi.org/10.1007/s00367-013-0321-7>
- Ivarsson, M., Broman, C., Sturkell, E., Örmö, J., Siljeström, S., van Zuijen, M., & Bengtson, S. (2013). Fungal colonization of an Ordovician impact-induced hydrothermal system. *Scientific Reports*, 3(1), 3487. <https://doi.org/10.1038/srep03487>
- Ivarsson, M., Drake, H., Neubeck, A., Sallstedt, T., Bengtson, S., Roberts, N. M. W., & Rasmussen, B. (2020). The fossil record of igneous rock. *Earth-Science Reviews*, 210, 103342. <https://doi.org/10.1016/j.earscirev.2020.103342>
- Ivarsson, M., Kiliias, S. P., Broman, C., Neubeck, A., Drake, H., Fru, E. C., et al. (2019). Exceptional preservation of fungi as H<sub>2</sub>-bearing fluid inclusions in an early Quaternary paleo-hydrothermal system at Cape Vani, Milos, Greece. *Minerals*, 9(12), 749. <https://doi.org/10.3390/min9120749>
- Ivarsson, M., Peckmann, J., Tehler, A., Broman, C., Bach, W., Behrens, K., et al. (2015). Zygomycetes in vesicular Basanites from Vesteris Seamouth, Greenland basin – a New type of Cryptoendolithic fungi. *PLoS One*, 10(7), e0133368. <https://doi.org/10.1371/journal.pone.0133368>
- Japsen, P., Bonow, J. M., Green, P. F., Chalmers, J. A., & Lidmar-Bergström, K. (2006). Elevated, passive continental margins: Long-term highs or Neogene uplifts? New evidence from west Greenland. *Earth and Planetary Science Letters*, 248(1–2), 330–339. <https://doi.org/10.1016/j.epsl.2006.05.036>
- Jess, S., Stephenson, R., & Brown, R. (2018). Evolution of the central West Greenland margin and the Nuussuaq Basin: Localised basin uplift along a stable continental margin proposed from thermochronological data. *Basin Research*, 30(6), 1230–1246. <https://doi.org/10.1111/bre.12301>
- Johansson, E., Gustafsson, L.-G., Berglund, S., Lindborg, T., Selroos, J.-O., Claesson Liljedahl, L., & Destouni, G. (2015). Data evaluation and numerical modeling of hydrological interactions between active layer, lake and talik in a permafrost catchment, Western Greenland. *Journal of Hydrology*, 527, 688–703. <https://doi.org/10.1016/j.jhydrol.2015.05.026>
- Johnston, D. T., Poulton, S. W., Fralick, P. W., Wing, B. A., Canfield, D. E., & Farquhar, J. (2006). Evolution of the oceanic sulfur cycle at the end of the Paleoproterozoic. *Geochimica et Cosmochimica Acta*, 70(23), 5723–5739. <https://doi.org/10.1016/j.gca.2006.08.001>
- Kaksonen, A. H., Spring, S., Schumann, P., Kroppenstedt, R. M., & Puhakka, J. A. (2006). Desulfotomaculum thermosubterraneum sp. nov., a thermophilic sulfate-reducer isolated from an underground mine located in a geothermally active area. *International Journal of Systematic and Evolutionary Microbiology*, 56(11), 2603–2608. <https://doi.org/10.1099/ijs.0.64439-0>



- Kiel, S., Glodny, J., Birgel, D., Bulot, L. G., Campbell, K. A., Gaillard, C., et al. (2014). The Paleocology, Habitats, and stratigraphic range of the enigmatic Cretaceous brachiopod *Peregrinella*. *PLoS One*, 9(10), e109260. <https://doi.org/10.1371/journal.pone.0109260>
- Kietäväinen, R., Ahonen, L., Kukkonen, I. T., Niedermann, S., & Wiersberg, T. (2014). Noble gas residence times of saline waters within crystalline bedrock, Outokumpu Deep Drill Hole, Finland. *Geochimica et Cosmochimica Acta*, 145, 159–174. <https://doi.org/10.1016/j.gca.2014.09.012>
- Kim, S.-T., & O'Neil, J. R. (1997). Equilibrium and nonequilibrium oxygen isotope effects in synthetic carbonates. *Geochimica et Cosmochimica Acta*, 61(16), 3461–3475. [https://doi.org/10.1016/s0016-7037\(97\)00169-5](https://doi.org/10.1016/s0016-7037(97)00169-5)
- Kiyosu, Y., & Krouse, H. R. (1990). The role of organic acid in the abiogenic reduction of sulfate and the sulfur isotope effect. *Geochemical Journal*, 24(1), 21–27. <https://doi.org/10.2343/geochemj.24.21>
- Klint, K. E. S., Engström, J., Parmenter, A., Ruskeeniemi, T., Claesson Liljedahl, L., & Lehtinen, A. (2013). Lineament mapping and geological history of the Kangerlussuaq region, southern West Greenland. *GEUS Bulletin*, 28, 57–60. <https://doi.org/10.34194/geusb.v28.4725>
- Leavitt, W. D., Halevy, I., Bradley, A. S., & Johnston, D. T. (2013). Influence of sulfate reduction rates on the Phanerozoic sulfur isotope record. *Proceedings of the National Academy of Sciences*, 110(28), 11244–11249. <https://doi.org/10.1073/pnas.1218874110>
- Liljedahl, L. C., Meierbachtol, T., Harper, J., van As, D., Näslund, J.-O., Selroos, J.-O., et al. (2021). Rapid and sensitive response of Greenland's groundwater system to ice sheet change. *Nature Geoscience*, 14(10), 751–755. <https://doi.org/10.1038/s41561-021-00813-1>
- Lima-Zaloumis, J., Neubeck, A., Ivarsson, M., Bose, M., Greenberger, R., Templeton, A. S., et al. (2022). Microbial biosignature preservation in carbonated serpentinite from the Samail Ophiolite, Oman. *Communications Earth & Environment*, 3(1), 231. <https://doi.org/10.1038/s43247-022-00551-1>
- Liseroudi Mastaneh, H., Ardakani, O. H., Pedersen, P. K., Stern, R. A., Wood, J. M., & Sanei, H. (2021). Microbial and thermochemical controlled sulfur cycle in the Early Triassic sediments of the Western Canadian Sedimentary Basin. *Journal of the Geological Society*, 178(4), jgs20202175. <https://doi.org/10.1144/jgs2020-175>
- Lundin, E. R., & Doré, A. G. (2005). Fixity of the Iceland “hotspot” on the Mid-Atlantic Ridge: Observational evidence, mechanisms, and implications for Atlantic volcanic margins. In G. R. Foulger, J. H. Natland, D. C. Presnall, & D. L. Anderson (Eds.), *Plates, plumes and paradigms*. Geological Society of America.
- Machel, H. G., Krouse, H. R., & Sassen, R. (1995). Products and distinguishing criteria of bacterial and thermochemical sulfate reduction. *Applied Geochemistry*, 10(4), 373–389. [https://doi.org/10.1016/0883-2927\(95\)00008-8](https://doi.org/10.1016/0883-2927(95)00008-8)
- Magnall, J. M., Gleeson, S. A., Stern, R. A., Newton, R. J., Poulton, S. W., & Paradis, S. (2016). Open system sulphate reduction in a diagenetic environment – Isotopic analysis of barite ( $\delta^{34}\text{S}$  and  $\delta^{18}\text{O}$ ) and pyrite ( $\delta^{34}\text{S}$ ) from the Tom and Jason Late Devonian Zn–Pb–Ba deposits, Selwyn Basin, Canada. *Geochimica et Cosmochimica Acta*, 180, 146–163. <https://doi.org/10.1016/j.gca.2016.02.015>
- Marker, M., Mengel, F., van Gool, J., & Field Party (1995). Evolution of the Palaeoproterozoic Nagssugtoqidian orogen: DLC investigations in West Greenland. *Rapport Grønlands Geologiske Undersøgelse*, 165, 100–105. <https://doi.org/10.34194/rapgg.v165.8288>
- Martini, A. M., Walter, L. M., Budai, J. M., Ku, T. C. W., Kaiser, C. J., & Schoell, M. (1998). Genetic and temporal relations between formation waters and biogenic methane: Upper Devonian Antrim Shale, Michigan Basin, USA. *Geochimica et Cosmochimica Acta*, 62(10), 1699–1720. [https://doi.org/10.1016/s0016-7037\(98\)00090-8](https://doi.org/10.1016/s0016-7037(98)00090-8)
- McIntosh, J., Kim, J.-H., Bailey, L., Osburn, M., Drake, H., Martini, A., et al. (2023). Burial and denudation alter microbial life at the bottom of the hypo-critical zone. *Geochemistry, Geophysics, Geosystems*, 24(6), e2022GC010831. <https://doi.org/10.1029/2022gc010831>
- Melchior Larsen, L., Rex, D. C., Watt, W. S., & Guise, P. G. (1999).  $^{40}\text{Ar}$ – $^{39}\text{Ar}$  dating of alkali basaltic dykes along the southwest coast of Greenland: Cretaceous and Tertiary igneous activity along the eastern margin of the Labrador Sea. *Geology of Greenland Survey Bulletin*, 184, 19–29. <https://doi.org/10.34194/ggub.v184.5227>
- Milodowski, A. E., Bath, A., & Norris, S. (2018). Palaeohydrogeology using geochemical, isotopic and mineralogical analyses: Salinity and redox evolution in a deep groundwater system through Quaternary glacial cycles. *Applied Geochemistry*, 97, 40–60. <https://doi.org/10.1016/j.apgeochem.2018.07.008>
- Mizuno, T., Suzuki, Y., Milodowski, A. E., & Iwatsuki, T. (2023). Isotopic signals in fracture-filling calcite showing anaerobic oxidation of methane in a granitic basement. *Applied Geochemistry*, 150, 105571. <https://doi.org/10.1016/j.apgeochem.2023.105571>
- Mokadem, F., Parkinson, I. J., Hathorne, E. C., Anand, P., Allen, J. T., & Burton, K. W. (2015). High-precision radiogenic strontium isotope measurements of the modern and glacial ocean: Limits on glacial–interglacial variations in continental weathering. *Earth and Planetary Science Letters*, 415, 111–120. <https://doi.org/10.1016/j.epsl.2015.01.036>
- Noe-Nygaard, A., & Ramberg, H. (1961). Geological reconnaissance map of the Country between Latitudes 69°N and 63°45' N, west Greenland. *Meddelelser om Grønland*, 124, 1–9.
- Nutman, A. P., Kalsbeek, F., Marker, M., van Gool, J. A. M., & Bridgwater, D. (1999). U–Pb zircon ages of Kangamiut dykes and detrital zircons in metasediments in the Palaeoproterozoic Nagssugtoqidian Orogen (West Greenland): Clues to the pre-collisional history of the orogen. *Precambrian Research*, 93(1), 87–104. [https://doi.org/10.1016/s0301-9268\(98\)00099-0](https://doi.org/10.1016/s0301-9268(98)00099-0)
- Oakes, C. S., Bodnar, R. J., & Simonson, J. M. (1990). The system  $\text{NaCl}$ – $\text{CaCl}_2$ – $\text{H}_2\text{O}$ : I. The ice liquidus at 1 atm total pressure. *Geochimica et Cosmochimica Acta*, 54(3), 603–610. [https://doi.org/10.1016/0016-7037\(90\)90356-p](https://doi.org/10.1016/0016-7037(90)90356-p)
- O'Neil, J. R., Clayton, R. N., & Mayeda, T. K. (1969). Oxygen isotopic fractionation in divalent metal carbonates. *Journal of Chemical Physics*, 51(12), 5547–5558. <https://doi.org/10.1063/1.1671982>
- Osterholz, H., Turner, S., Alakangas, L. J., Tullborg, E.-L., Dittmar, T., Kalinowski, B. E., & Dopson, M. (2022). Terrigenous dissolved organic matter persists in the energy-limited deep groundwaters of the Fennoscandian Shield. *Nature Communications*, 13(1), 4837. <https://doi.org/10.1038/s41467-022-32457-z>
- Parnell, J., Boyce, A., Thackrey, S., Muirhead, D., Lindgren, P., Mason, C., et al. (2010). Sulfur isotope signatures for rapid colonization of an impact crater by thermophilic microbes. *Geology*, 38(3), 271–274. <https://doi.org/10.1130/g30615.1>
- Paul, D., & Skrzypek, G. (2007). Assessment of carbonate-phosphoric acid analytical technique performed using GasBench II in continuous flow isotope ratio mass spectrometry. *International Journal of Mass Spectrometry*, 262(3), 180–186. <https://doi.org/10.1016/j.ijms.2006.11.006>
- Pedersen, K., Bengtsson, A. F., Edlund, J. S., & Eriksson, L. C. (2014). Sulphate-controlled diversity of subterranean microbial communities over depth in deep groundwater with opposing gradients of sulphate and methane. *Geomicrobiology Journal*, 31(7), 617–631. <https://doi.org/10.1080/01490451.2013.879508>
- Pedersen, K., Ekendahl, S., Tullborg, E.-L., Furnes, H., Thorseth, I., & Tumor, O. (1997). Evidence of ancient life at 207 m depth in a granitic aquifer. *Geology*, 25(9), 827–830. [https://doi.org/10.1130/0091-7613\(1997\)025<0827:eoalam>2.3.co;2](https://doi.org/10.1130/0091-7613(1997)025<0827:eoalam>2.3.co;2)
- Pere, T. (2014). Geological logging of the Greenland analogue project drill Croes DH-GAP01, 03, and 04. In *Posiva working report 2013-59*. Posiva Oy.
- Pitkänen, P., Partamies, S., Lahdenperä, A.-M., Ahokas, T., & Lamminmäki, T. (2009). *Results of monitoring at Olkiluoto in 2008; Hydro-geochemistry*. Posiva Oy.

- Pöllänen, J., Heikkinen, P., & Lehtinen, A. (2012). Difference flow measurements in Greenland, Drillhole DH-GAP04 in July 2011. In *SKB report*.
- Potter, R. W., Clyne, M. A., & Brown, D. L. (1978). Freezing-point depression of aqueous sodium chloride solutions. *Economic Geology*, 73(2), 284–285. <https://doi.org/10.2113/gsecongeo.73.2.284>
- Present, T. M., Adkins, J. F., & Fischer, W. W. (2020). Variability in sulfur isotope records of Phanerozoic seawater sulfate. *Geophysical Research Letters*, 47(18), e2020GL088766. <https://doi.org/10.1029/2020gl088766>
- Ren, S., Faleide, J. I., Eldholm, O., Skogseid, J., & Gradstein, F. (2003). Late Cretaceous–Paleocene tectonic development of the NW Vøring basin. *Marine and Petroleum Geology*, 20(2), 177–206. [https://doi.org/10.1016/s0264-8172\(03\)00005-9](https://doi.org/10.1016/s0264-8172(03)00005-9)
- Roberts, N. M. W., Rasbury, E. T., Parrish, R. R., Smith, C. J., Horstwood, M. S. A., & Condon, D. J. (2017). A calcite reference material for LA-ICP-MS U-Pb geochronology. *Geochemistry, Geophysics, Geosystems*, 18(7), 2807–2814. <https://doi.org/10.1002/2016gc006784>
- Roberts, N. W., & Walker, R. J. (2016). U-Pb geochronology of calcite mineralized faults; absolute dating of rift-related fault events on the northeast Atlantic margin. *Geology*, 44(7), 531–534. <https://doi.org/10.1130/g37868.1>
- Roedder, E. (1984). Fluid inclusions. In *Reviews in mineralogy*. Mineralogical Society of America.
- Ruskeeniemi, T., Engström, J., Lehtimäki, J., Vanhala, H., Korhonen, K., Kontula, A., et al. (2018). Subglacial permafrost evidencing re-advance of the Greenland Ice Sheet over frozen ground. *Quaternary Science Reviews*, 199, 174–187. <https://doi.org/10.1016/j.quascirev.2018.09.002>
- Sahlstedt, E., Karhu, J. A., & Pitkänen, P. (2010). Indications for the past redox environments in deep groundwaters from the isotopic composition of carbon and oxygen in fracture calcite, Olkiluoto, SW Finland. *Isotopes in Environmental and Health Studies*, 46(3), 370–391. <https://doi.org/10.1080/10256016.2010.505981>
- Sahlstedt, E., Karhu, J. A., Pitkänen, P., & Whitehouse, M. (2013). Implications of sulfur isotope fractionation in fracture-filling sulfides in crystalline bedrock, Olkiluoto, Finland. *Applied Geochemistry*, 32, 52–69. <https://doi.org/10.1016/j.apgeochem.2012.10.021>
- Sahlstedt, E., Karhu, J. A., Pitkänen, P., & Whitehouse, M. (2016). Biogenic processes in crystalline bedrock fractures indicated by carbon isotope signatures of secondary calcite. *Applied Geochemistry*, 67, 30–41. <https://doi.org/10.1016/j.apgeochem.2016.01.010>
- Sánchez-Andrea, I., Stams, A. J. M., Hedrich, S., Nancuccho, I., & Johnson, D. B. (2015). *Desulfosporosinus acididurans* sp. nov. an acidophilic sulfate-reducing bacterium isolated from acidic sediments. *Extremophiles*, 19(1), 39–47. <https://doi.org/10.1007/s00792-014-0701-6>
- Sandström, B., & Tullborg, E.-L. (2009). Episodic fluid migration in the Fennoscandian Shield recorded by stable isotopes, rare Earth elements and fluid inclusions in fracture minerals at Forsmark, Sweden. *Chemical Geology*, 266(3–4), 126–142. <https://doi.org/10.1016/j.chemgeo.2009.04.019>
- Sandström, B., Tullborg, E.-L., Larson, S. Å., & Page, L. (2009). Brittle tectonothermal evolution in the Forsmark area, central Fennoscandian Shield, recorded by paragenesis, orientation and  $^{40}\text{Ar}/^{39}\text{Ar}$  geochronology of fracture minerals. *Tectonophysics*, 478(3–4), 158–174. <https://doi.org/10.1016/j.tecto.2009.08.006>
- Seitsamo-Ryynänen, M., Karhu, J. A., Pitkänen, P., & Whitehouse, M. (2022). Isotopic signatures of present-day calcite and pyrite in low-temperature crystalline bedrock, Olkiluoto, SW Finland. *Applied Geochemistry*, 141, 105308. <https://doi.org/10.1016/j.apgeochem.2022.105308>
- Shepherd, T. J., Rankin, A. H., & Alderton, D. H. M. (1985). *A practical guide to fluid inclusion studies*. Blackie.
- Sim, M. S., Bosak, T., & Ono, S. (2011). Large sulfur isotope fractionation does not require disproportionation. *Science*, 333(6038), 74–77. <https://doi.org/10.1126/science.1205103>
- Simpson, S. L., Boyce, A. J., Lambert, P., Lindgren, P., & Lee, M. R. (2017). Evidence for an impact-induced biosphere from the  $\delta^{34}\text{S}$  signature of sulphides in the Rochechouart impact structure, France. *Earth and Planetary Science Letters*, 460, 192–200. <https://doi.org/10.1016/j.epsl.2016.12.023>
- So, C. M., & Young, L. Y. (1999). Initial reactions in anaerobic alkane degradation by a sulfate reducer, strain AK-01. *Applied and Environmental Microbiology*, 65(12), 5532–5540. <https://doi.org/10.1128/aem.65.12.5532-5540.1999>
- Stotler, R. L., Frapé, S. K., Ruskeeniemi, T., Ahonen, L., Onstott, T. C., & Hobbs, M. Y. (2009). Hydrogeochemistry of groundwaters in and below the base of thick permafrost at Lupin, Nunavut, Canada. *Journal of Hydrology*, 373(1–2), 80–95. <https://doi.org/10.1016/j.jhydrol.2009.04.013>
- Stotler, R. L., Frapé, S. K., Ruskeeniemi, T., Pitkänen, P., & Blowes, D. W. (2012). The interglacial–glacial cycle and geochemical evolution of Canadian and Fennoscandian Shield groundwaters. *Geochimica et Cosmochimica Acta*, 76, 45–67. <https://doi.org/10.1016/j.gca.2011.10.006>
- Takai, K., Nakamura, K., Toki, T., Tsunogai, U., Miyazaki, M., Miyazaki, J., et al. (2008). Cell proliferation at 122°C and isotopically heavy  $\text{CH}_4$  production by a hyperthermophilic methanogen under high-pressure cultivation. *Proceedings of the National Academy of Sciences*, 105(31), 10949–10954. <https://doi.org/10.1073/pnas.0712334105>
- Thiel, J., Byrne, J. M., Kappler, A., Schink, B., & Pester, M. (2019). Pyrite formation from FeS and  $\text{H}_2\text{S}$  is mediated through microbial redox activity. *Proceedings of the National Academy of Sciences*, 116(14), 6897–6902. <https://doi.org/10.1073/pnas.1814412116>
- Tillberg, M., Ivarsson, M., Drake, H., Whitehouse, J. M., Kooijman, E., & Schmitt, M. (2019). Re-evaluating the age of deep biosphere fossils in the lockne impact structure. *Geosciences*, 9(5), 202. <https://doi.org/10.3390/geosciences9050202>
- Tullborg, E.-L., Drake, H., & Sandström, B. (2008). Palaeohydrogeology: A methodology based on fracture mineral studies. *Applied Geochemistry*, 23(7), 1881–1897. <https://doi.org/10.1016/j.apgeochem.2008.02.009>
- Tullborg, E.-L., Landström, O., & Wallin, B. (1999). Low-temperature trace element mobility influenced by microbial activity; indications from fracture calcite and pyrite in crystalline basement. *Chemical Geology*, 157(3–4), 199–218. [https://doi.org/10.1016/s0009-2541\(99\)00002-9](https://doi.org/10.1016/s0009-2541(99)00002-9)
- Tuttas, D., & Schwieters, J. B. (2008). Advances in high precision isotope ratio measurements of calcium using TI-MS. *Thermo Fisher*.
- Ueki, A., & Suto, T. (1979). Cellular fatty acid composition of sulfate-reducing bacteria. *Journal of General and Applied Microbiology*, 25(3), 185–196. <https://doi.org/10.2323/jgam.25.185>
- Vermeech, P. (2018). IsoplotR: A free and open toolbox for geochronology. *Geoscience Frontiers*, 9(5), 1479–1493. <https://doi.org/10.1016/j.gsf.2018.04.001>
- Wallin, B., & Peterman, Z. (1999). Calcite fracture fillings as indicators of palaeohydrogeology at Laxemar at the Äspö Hard Rock Laboratory, southern Sweden. *Applied Geochemistry*, 14(7), 953–962. [https://doi.org/10.1016/s0883-2927\(99\)00028-1](https://doi.org/10.1016/s0883-2927(99)00028-1)
- Wang, J., Jacobson, A. D., Zhang, H., Ramezani, J., Sageman, B. B., Hurtgen, M. T., et al. (2019). Coupled  $\delta^{44/40}\text{Ca}$ ,  $\delta^{88/86}\text{Sr}$ , and  $\delta^{87}\text{Sr}/^{86}\text{Sr}$  geochemistry across the end-Permian mass extinction event. *Geochimica et Cosmochimica Acta*, 262, 143–165. <https://doi.org/10.1016/j.gca.2019.07.035>
- Westmeijer, G., Mehrshad, M., Turner, S., Alakangas, L., Sachpazidou, V., Bunse, C., et al. (2022). Connectivity of Fennoscandian Shield terrestrial deep biosphere microbiomes with surface communities. *Communications Biology*, 5(1), 37. <https://doi.org/10.1038/s42003-021-02980-8>

- Whitehouse, M. J. (2013). Multiple sulfur isotope determination by SIMS: Evaluation of reference sulfides for  $\Delta^{33}\text{S}$  with observations and a case study on the determination of  $\Delta^{36}\text{S}$ . *Geostandards and Geoanalytical Research*, 37(1), 19–33. <https://doi.org/10.1111/j.1751-908x.2012.00188.x>
- Wilson, R. W., Klint, K. E. S., van Gool, J. A. M., McCaffrey, K. J. W., Holdsworth, R. E., & Chalmers, J. A. (2006). Faults and fractures in central west Greenland: Onshore expression of continental break-up and sea-floor spreading in the Labrador – Baffin Bay sea. *GEUS Bulletin*, 11, 185–204. <https://doi.org/10.34194/geusb.v11.4931>
- Woodhead, J. D., & Hergt, J. M. (2001). Strontium, neodymium and lead isotope analyses of NIST glass certified reference materials: SRM 610, 612, 614. *Geostandards Newsletter*, 25(2–3), 261–266. <https://doi.org/10.1111/j.1751-908x.2001.tb00601.x>
- Wortmann, U. G., Bernasconi, S. M., & Böttcher, M. E. (2001). Hypersulfidic deep biosphere indicates extreme sulfur isotope fractionation during single-step microbial sulfate reduction. *Geology*, 29(7), 647–650. [https://doi.org/10.1130/0091-7613\(2001\)029<0647:hdbies>2.0.co;2](https://doi.org/10.1130/0091-7613(2001)029<0647:hdbies>2.0.co;2)